sustainability

MDPI

Article

Design of Nanostructured Sulfonated Polymeric Nanoparticles for Sustainable Cationic Dye Removal from Water

Tamer M. Tamer [1,*], Mohamed A. Hassan [2,*], Theodora Krasia-Christoforou [1], Mohamed S. Mohyeldin [3] and Ioannis Pashalidis [4]

1 Department of Mechanical and Manufacturing Engineering, University of Cyprus, P.O. Box 20537, 1678 Nicosia, Cyprus; krasia.theodora@ucy.ac.cy
2 Protein Research Department, Genetic Engineering and Biotechnology Research Institute (GEBRI), City of Scientific Research and Technological Applications (SRTA-City), New Borg El-Arab City, Alexandria 21934, Egypt
3 Polymer Materials Research Department, Advanced Technologies and New Materials Research Institute (ATNMRI), City of Scientific Research and Technological Applications (SRTA-City), New Borg El-Arab City, Alexandria 21934, Egypt; mmohyeldin@srtacity.sci.eg
4 Department of Chemistry, University of Cyprus, P.O. Box 20537, 1678 Nicosia, Cyprus; paschalidis.ioannis@ucy.ac.cy
* Correspondence: abdelrazik.tamer@ucy.ac.cy (T.M.T.); madel@srtacity.sci.eg (M.A.H.)

Abstract

The persistent discharge of cationic dyes into aquatic systems necessitates advanced adsorbents with precisely tunable interfacial properties and high removal efficiency. Herein, we report for the first time the synthesis of composition-controlled sulfonated polymeric nanoparticles (NPs) based on polystyrene (PSt) and poly(2-acrylamido-2-methyl-1-propanesulfonic acid) (PAMPS) via a surfactant-free precipitation polymerization approach. Our findings showed that the NPs exhibited well-defined composition-dependent evolution in physicochemical properties, with hydrodynamic size decreasing from 1224 to 327 nm and surface charge rising from −36.1 to −51.0 mV with increasing PAMPS content. Furthermore, adsorption performance toward methylene blue (MB) and crystal violet (CV) demonstrated strong dependence on surface charge density, with removal efficiencies of 97–98% at low initial dye concentrations (10–20 mg L^{-1}) and still above 82–87% at a higher initial concentration (100 mg L^{-1}). At low initial dye concentrations (10–20 mg L^{-1}), the most highly sulfonated nanoparticles (NP-PSt/AMPS-50) reach equilibrium capacities of approximately 9.25–971 mg g^{-1}, while at 100 mg L^{-1}, the capacities increase to about 82–86 mg g^{-1} for both MB and CV. Notably, the adsorption capacity (q_e) increases systematically with the sulfonation degree, reflecting enhanced ion-exchange capacity and accessibility of surface-exposed $–SO_3^-$ functionalities. Rapid uptake behavior is observed, with >60–70% removal achieved within 15 min and equilibrium established within 100–120 min. Importantly, the enhanced adsorption performance of NPs can be attributed to their self-organized core–shell-like architecture. Considering this structure, hydrophobic PSt-rich domains form the particle interior, while PAMPS segments are localized at particle–water interface, creating a sulfonate-enriched surface layer. This enhances active-site accessibility and electrostatic interactions with cationic dyes. The composition-dependent evolution of sulfonate functional groups, as evidenced by FTIR spectroscopy, along with the systematic decrease in hydrodynamic size and increase in zeta potential magnitude with increasing AMPS content, collectively indicate the surface localization of charged PAMPS segments. Overall, our findings provide a mechanistic framework for the rational design of charge-regulated polymeric nano adsorbents and highlight the potential of PSt/PAMPS NPs as scalable and sustainable materials for cationic dye removal in wastewater treatment systems.

Check for updates

Academic Editor: Charikleia Prochaska

Received: 7 May 2026
Revised: 20 June 2026
Accepted: 26 June 2026
Published: 1 July 2026

Copyright: © 2026 by the authors. Licensee MDPI, Basel, Switzerland. This article is an open access article distributed under the terms and conditions of the Creative Commons Attribution (CC BY) license.

Keywords: sulfonated polymeric nanoparticles; polystyrene–PAMPS copolymers; cationic dye removal; methylene blue; crystal violet; wastewater treatment; sustainable sorbents

1. Introduction

The continuous discharge of synthetic dyes from the textile, leather, pharmaceutical and polymer-processing industries constitutes a major environmental concern, owing to their persistence, high chromaticity and resistance to natural degradation pathways. Once released into aquatic systems, these compounds significantly impair light penetration, disrupt photosynthetic, activity and increase chemical oxygen demand, thereby destabilizing aquatic ecosystems and posing risks to human health [1–3]. Among the diverse classes of dyes, cationic species such as methylene blue (MB) and crystal violet (CV) are particularly problematic due to their strong aromatic frameworks, high aqueous, stability and well-documented toxicological effects, including mutagenicity and potential carcinogenicity even at low concentrations [4,5]. Consequently, the development of efficient and selective strategies for their removal remains a critical priority in advanced water treatment technologies [6].

Conventional remediation approaches, including coagulation–flocculation, membrane separation, biological, degradation and advanced oxidation, often suffer from intrinsic limitations such as low selectivity, high operational costs, secondary waste, generation and incomplete mineralization of recalcitrant dye molecules [7,8]. In this context, adsorption has emerged as a highly attractive alternative due to its operational simplicity, scalability and high removal efficiency. However, its practical implementation remains strongly dependent on the physicochemical characteristics of the adsorbent, particularly surface functionality, charge density, accessibility to active, sites and structural stability under varying environmental conditions [9,10].

Polymeric materials functionalized with ionizable groups have recently gained significant attention as advanced adsorbent platforms, owing to their tunable molecular architecture and versatility in form. Among them, sulfonated polymers are especially promising due to the presence of permanently ionized sulfonate ($–SO_3^-$) groups, which impart strong electrostatic affinity for cationic pollutants, high hydrophilicity, and excellent chemical stability across a wide pH range [11,12]. Nevertheless, conventional bulk sulfonated polymers are often impeded by restricted surface area and slow intraparticle diffusion, leading to suboptimal adsorption kinetics and incomplete utilization of active sites [13].

While AMPS-based hydrogels and sulfonated polymer networks have been widely studied, these systems are often constrained by diffusion-limited transport and poorly defined surface charge distribution. Beyond conventional sulfonated resins, a diverse array of AMPS-based hydrogels, cryogels, and nanocomposite networks have been developed as adsorbents for cationic dyes, utilizing a combination of electrostatic attraction, ion exchange, and, on occasion, π–π and hydrogen-bonding interactions. AMPS-containing cryogel systems, including magnetically responsive Na-VS/Na-AMPS cryogel nanocomposites designed for MB removal, have shown that highly swollen, macroporous networks can enable rapid mass transfer and significant uptake capacity while maintaining structural stability over multiple adsorption–desorption cycles [14–17]. Nevertheless, these hydrogel- and cryogel-based platforms typically utilize bulk, percolating networks where active sites are dispersed within a relatively thick hydrated matrix. Consequently, adsorption kinetics can still be constrained by intragel diffusion, particularly at high dye loadings [18–20].

It is widely recognized that several PAMPS-containing hydrogels and cryogels have been reported as efficient adsorbents for cationic dyes, but they generally require relatively long contact times to reach equilibrium. A pAMPS-Na-co-VIm hydrogel and its Ag-nanocomposite, for example, removed rhodamine B from aqueous solution with adsorption capacities of about 36–55 mg g^{-1} as the initial concentration increased from 10 to 80 mg L^{-1}, and equilibrium was only reached after approximately 4 h of contact, reflecting slow intragel diffusion of the cationic dye through the crosslinked PAMPS network. Likewise, chitosan-based hydrogels grafted with poly(acrylic acid-co-AMPS) exhibit very high equilibrium uptakes for crystal violet (reported qmax $\approx$ 2500 mg g^{-1}) and methylene blue/other cationic dyes often in the 800–2000 mg g^{-1} range at high initial dye concentrations ($\sim$1000–3000 mg L^{-1}), but removal of 90–95% of crystal violet requires prolonged contact (12–16 h) and the pseudo-second-order rate constants are relatively low, indicating that mass transport within the swollen hydrogel matrix limits the overall adsorption rate. More recently, a dual-network chitosan hydrogel (CMAPP) achieved maximum capacities of roughly 1800–2500 mg g^{-1} for various cationic dyes at initial concentrations around 500 mg L^{-1} yet the time to reach adsorption equilibrium remained on the order of 400–700 min depending on the dye, with adsorption kinetics best described by a pseudo-second-order model dominated by chemisorption and intra-particle diffusion [14,15,17,21]. These previous reports not only collectively highlight the strong affinity of AMPS/PAMPS-containing and -related chitosan-based hydrogel networks for cationic dyes but also underscore common challenges, involving slow internal mass transport across micron scale and percolating hydrogel domains, which necessitate long contact times to fully exploit their high density of sulfonate and carboxylate adsorption sites.

In this context, nanotechnology has emerged as an innovative approach with broad applications in various environmental, agricultural, and biomedical fields, providing effective solutions to overcome the limitations of conventional materials and processes [22–25]. Therefore, nanostructuring has gained considerable attention as an effective strategy to promote adsorption performance by enhancing the surface-to-volume ratio, minimizing diffusion resistance, and maximizing the exposure of functional groups. In particular, sulfonated polymeric NPs provide a unique integration of high surface charge density, accessible ion-exchange sites, and tunable composition, enabling precise control over adsorption behavior at the nanoscale [26,27]. Among these materials, copolymer systems based on polystyrene (PSt) and poly(2-acrylamido-2-methyl-1-propanesulfonic acid) (PAMPS) represent an attractive platform, where the hydrophobic PSt backbone ensures structural integrity, while PAMPS introduces highly acidic sulfonate functionalities with superior ion-exchange capacity.

Despite the recognized potential of sulfonated styrene-based systems, understanding how copolymer composition governs NP structure, surface charge evolution, ion-exchange capacity and adsorption thermodynamics for cationic dyes remains limited. In particular, clear correlations between composition-dependent interfacial properties and adsorption kinetics or thermodynamics are lacking. In light of above, the current work seeks to investigate how the systematic variation of PSt/PAMPS copolymer composition in precipitation-polymerized nanoparticles influences their nanoscale architecture and surface charge, and how these interfacial properties govern the adsorption behavior of representative cationic dyes (MB and CV). In parallel, we explore how these structure-charge and function relationships can be leveraged to design crosslinked, surfactant-free PSt/PAMPS nanoparticles as promising, scalable sorbents for cationic dye removal from water, without yet performing full process-level optimization or long-term testing. To this end, we synthesize a composition series of PSt/PAMPS sulfonated polymeric NPs, characterize their morphology, colloidal properties and ion-exchange capacity, and evaluate their

equilibrium adsorption performance and pH/temperature dependence toward MB and CV under batch conditions. Additionally, their adsorption performance toward MB and CV was systematically evaluated under varying conditions (contact time, temperature, dye concentration and pH), and the adsorption behavior was interpreted qualitatively in terms of composition-dependent surface charge and nanoscale architecture, while detailed kinetic and thermodynamic modeling is reserved for future work. To the best of our knowledge, this study is the first to show the potential application of these nanostructured sulfonated polymeric NPs (PSt/PAMPS) varying feed ratios for the removal of cationic dyes from water, serving as a sustainable approach for water remediation. These findings provide mechanistic insights and a rational design framework for the fabrication of next-generation charge-regulated polymeric nano-adsorbents in wastewater remediation.

2. Materials and Methods

2.1. Materials

Styrene (St, 99%) and sodium 2-acrylamido-2-methylpropanesulfonate (AMPS-Na, 98%) were purchased from Sigma-Aldrich (St. Louis, MO, USA) and used as received without further purification, N,N′-methylenebisacrylamide (MBAA, ≥99%), and potassium persulfate (KPS, ≥99%) were purchased from Sigma-Aldrich and used as received without further purification. Absolute ethanol (EtOH, ≥99.8%, HPLC grade) and deionized water (18.2 MΩ·cm) were employed as the mixed solvent system for precipitation polymerization and NPs dispersion. Crystal Violet ($C_{25}H_{30}ClN_3$, molecular weight = 407.99 g·mol^{-1}) was purchased from Tokyo Chemical Industry Co., Ltd. (TCI, Tokyo, Japan) and used as the cationic dye model compound. Methylene blue (analytical grade) was obtained from Carlo Erba Reagenti (Cornaredo, Milan, Italy) and employed as a second representative cationic dye for adsorption studies.

2.2. Synthesis of Polymeric NPs

Polymeric NPs were synthesized by surfactant-free precipitation polymerization in an ethanol–water mixed solvent (EtOH:H_2O = 70:30 v/v) (Figure 1). Polymerization was conducted at 70 °C for 6 h with magnetic stirring. Five samples were prepared, namely crosslinked polystyrene (NP-PSt), crosslinked PAMPS (NP-PAMPS), and three PSt/PAMPS copolymers with nominal compositions of 90:10 (NP-PSt/AMPS-10), 70:30 (NP-PSt/AMPS-30), and 50:50 (NP-PSt/AMPS-50). In all formulations, potassium persulfate (KPS, 0.05 g) was employed as the radical initiator and N,N′-methylenebisacrylamide (MBAA, 0.05 g) as the crosslinking agent. (MBAA) was employed as a covalent crosslinker to ensure formation of insoluble, crosslinked nanoparticle networks and to minimize polymer dissolution under the aqueous adsorption conditions. For NP-PSt, 1.1 mL of styrene was polymerized in the same solvent mixture and initiation with KPS, yielding ~0.657 g of dry NPs (in average ~62.8% yield). NP-PAMPS was prepared by polymerizing 1.0 g of AMPS under identical conditions, affording 0.905 g of product (86.2% yield).

Copolymer NPs were synthesized using 0.99 mL styrene and 0.10 g AMPS for NP-PSt/AMPS-10, 0.77 mL styrene and 0.30 g AMPS for NP-PSt/AMPS-30 and 0.55 mL styrene and 0.50 g AMPS for NP-PSt/AMPS-50. The recovered dry masses were 0.7075 g (67.6% yield), 0.7484 g (71.4% yield) and 0.761 g (69.1% yield), respectively. The relatively high gravimetric yields (~63–86%) obtained for all PSt/PAMPS formulations further support the scalability of the surfactant-free precipitation polymerization route. All products were isolated by centrifugation, washed repeatedly with ethanol and deionized water, and dried under vacuum prior to characterization and adsorption experiments.

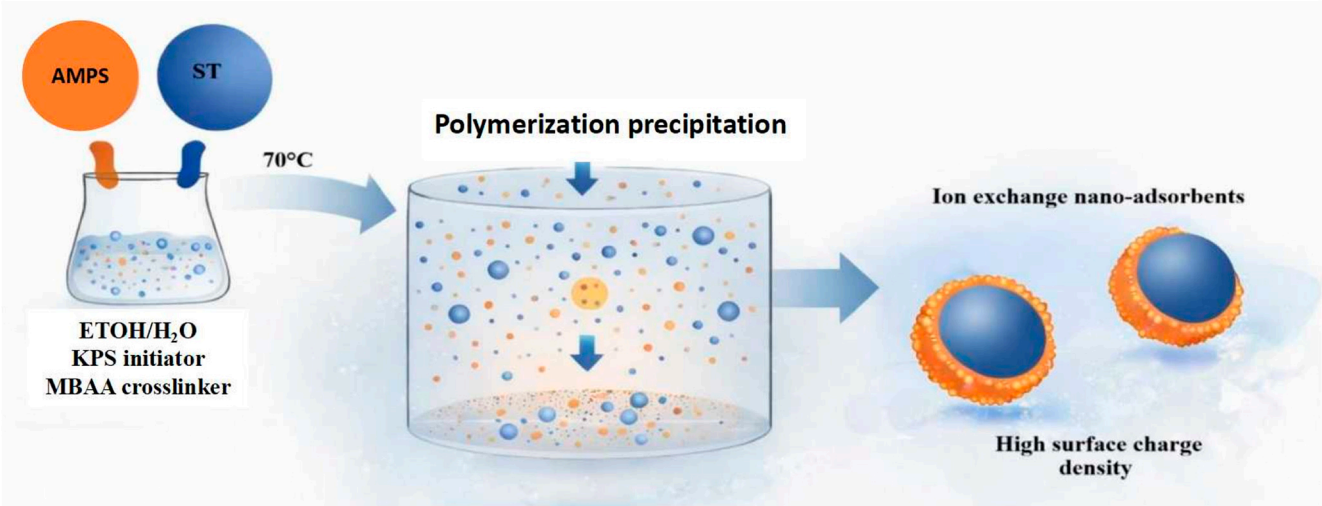

Figure 1. Schematic representation of the precipitation polymerization route employed for the synthesis of sulfonated polystyrene-based NPs.

2.3. Characterization

2.3.1. Fourier-Transform Infrared Spectroscopy (FT-IR)

FT-IR spectroscopy was used to verify the chemical structure of the synthesized NPs and to confirm the incorporation of sulfonic functional groups. Spectra were recorded using a Jasco FTIR 4100 (JASCO INTERNATIONAL Co., Ltd., Tokyo, Japan) over the range 4000–500 cm^{-1}.

2.3.2. Scanning Electron Microscopic Analysis (SEM)

The morphology and surface characteristics of the synthesized polymeric NPs were examined using scanning electron microscopy (SEM) Vega TS5136LS-Tescan (Tescan, Brno, Czech Republic). Prior to imaging, the dried samples were deposited onto aluminum stubs using conductive carbon tape and sputter-coated with a thin gold layer to prevent charging effects. The particle size distribution of NPs was determined using ImageJ Fiji software (https://imagej.net/software/fiji/downloads, accessed on 1 May 2026). Each image was firstly calibrated using the corresponding scale bar values and 70–80 NPs were then measured. The average particle size was reported as mean ± standard deviation (SD).

2.3.3. Thermal Gravimetric Analysis (TGA)

Thermogravimetric analysis was carried out to evaluate the thermal stability and degradation behavior of the synthesized NPs using a TGA Q50 analyzer (Version 20.13, Build 39) (TA Instruments, New Castle, DE, USA). The measurements were performed under a continuous nitrogen atmosphere by heating the samples from room temperature to 800 °C at a constant heating rate of 10 °C min^{-1}. The obtained thermograms were used to identify the main weight-loss events associated with moisture desorption, decomposition of the polymer backbone and degradation of sulfonated functionalities, providing insight into the influence of copolymer composition on thermal stability.

2.3.4. Determination of Ion-Exchange Capacity (IEC)

The ion-exchange capacity (IEC) of the PSt/PAMPS nanoparticles was determined by acid-based back-titration and expressed in milliequivalents per gram of dry polymer (meq g^{-1}). Dried nanoparticles (50–100 mg) were first converted to the H^+ form by stirring in 50 mL of 1.0 M HCl at room temperature for 24 h, followed by filtration, thorough washing with deionized water until the filtrate reached neutral pH, and vacuum-drying at

40 °C to constant mass. For IEC measurement, approximately 50 mg of the H^+ form sample was soaked in 50.0 mL of standardized 0.10 M NaOH solution for 24 h at room temperature, then filtered. An aliquot (25.0 mL) of the filtrate was back-titrated with standardized 0.10 M HCl using phenolphthalein as indicator; a blank without polymer was treated identically. IEC was calculated from the difference between the HCl volumes consumed in blank and sample titrations using Equation (1):

$$IEC\left(\frac{\text{meq}}{\text{g}}\right) = \frac{\left(V_{blank} - V_{sample}\right)}{m_{dry}} \times C_{HCl} \quad (1)$$

where V_{blank} and V_{sample} are the HCl volumes (mL), C_{HCl} is the HCl concentration (mol L^{-1}), and m_{dry} is the mass (g) of dried polymer. IEC values are reported as mean ± standard deviation from triplicate measurements.

2.3.5. Zeta Potential Measurements

Zeta potential measurements were performed using electrophoretic light scattering (ELS) on a Zetasizer instrument (Malvern Panalytical Ltd., Malvern, UK) equipped with a laser Doppler velocimetry module. Nanoparticle dispersions were prepared by dispersing the dried powders in deionized water (18.2 MΩ·cm) and sonicating for 10–15 min to ensure homogeneous suspensions. Dispersions were adjusted to pH 6.5 ± 0.2 prior to measurement, and the particle concentration was fixed at 0.1 mg mL^{-1}. Zeta potential measurements were performed at pH 6.5 ± 0.2, which corresponds to the near-neutral conditions used in the majority of the kinetic and isotherm experiments and ensures optimal colloidal stability of the dispersions. Measurements were conducted at 25 ± 0.1 °C using disposable folded capillary cells (DTS1070).

The reported zeta potential values were calculated from the measured electrophoretic mobility using the Smoluchowski approximation, which is appropriate for aqueous media of moderate ionic strength. For each sample, at least three independent measurements were performed (≥10–12 runs per measurement), and the results are presented as mean ± standard deviation. Conductivity and pH of the dispersions were recorded during analysis, and all samples were measured under identical dispersion conditions to ensure valid comparison across compositions.

2.4. Batch Adsorption Experiments

The adsorption performance of the synthesized NPs was evaluated in batch mode using Methylene Blue (MB) and Crystal Violet (CV) as model cationic dyes. Stock dye solutions (1000 mg L^{-1}) were prepared in deionized water and diluted to the desired concentrations prior to each experiment. Adsorption tests were conducted by adding a known mass of dried (1–5 mg) NPs to a fixed volume of dye solution (2–10 mL) in sealed flasks and agitating the suspensions at a constant shaking speed in a thermostatically controlled shaker. The effects of contact time, initial dye concentration, solution pH adsorbent dose, and temperature on the adsorption behavior were systematically investigated. Solution pH was adjusted using dilute HCl or NaOH (0.1 M) and monitored throughout the experiments. At predetermined time intervals, aliquots were withdrawn, centrifuged to separate the adsorbent and the residual dye concentration in the supernatant was determined by UV–Vis spectrophotometry (Jasco V-630, JASCO International Co., Ltd., Tokyo, Japan) at the characteristic maximum absorption wavelengths of MB (λmax = 664 nm) and CV (λmax = 590 nm). Control experiments were performed under identical conditions but in the absence of nanoparticles to verify the stability of MB and CV solutions. All calculations were performed using Equations (2)–(4). No significant change in absorbance (<2%) was

observed over the maximum contact time, confirming negligible dye degradation or losses to the reactor walls under the experimental conditions.

$$qt = \frac{(C_0 - C_t)V}{m} \tag{2}$$

$$qe = \frac{(C_0 - C_e)V}{m} \tag{3}$$

$$Removing\ rate\ (\%) = \frac{(C_0 - C_t)}{C_0} \times 100 \tag{4}$$

where C_0, C_t, and C_e (mg L^{-1}) are the initial, time-dependent and equilibrium dye concentrations, respectively, V (L) is the solution volume and m (g) is the mass of adsorbent.

2.5. Reusability and Regeneration Tests

The reusability of the PSt/PAMPS nanoparticles was evaluated over five successive adsorptions–desorption cycles using MB and CV as model dyes. After each adsorption run, the nanoparticle dispersions were centrifuged to recover the spent adsorbent, and the supernatant was decanted. The recovered nanoparticles were then resuspended in 5 mL of absolute ethanol and stirred for 1 h to desorb the retained dye. The suspension was centrifuged again, the ethanol phase was discarded, and the particles were washed three times one time with Saline solution and two times with deionized water and re-dispersed in fresh dye solution for the next cycle. The removal efficiency in each cycle was determined under the same initial dye concentration, adsorbent dose, and contact time as in the first run, allowing assessment of the retention of adsorption performance upon repeated use.

2.6. Statistical Analysis

All experiments assessing the effects of various parameters on the removal of Crystal Violet (CV) and Methylene Blue (MB) by PSt/PAMPS NPs were conducted in triplicate. Statistical analysis was performed employing two-way analysis of variance (ANOVA) with Tukey's post hoc test in GraphPad Prism (Version 8, GraphPad Software Inc., Boston, MA, USA). Data are illustrated as mean ± standard deviation (SD), and differences were considered statistically significant at $p < 0.05$.

3. Results

The polymeric NPs were fabricated by a surfactant-free precipitation polymerization approach, which exploits the limited solubility of the growing polymer chains in a mixed ethanol–water medium to induce controlled phase separation and NP formation. In this solvent system, the monomers are initially molecularly dispersed, whereas the progressive increase in molecular weight during polymerization leads to a gradual loss of solubility and spontaneous nucleation of polymer-rich domains. This solvent-driven precipitation process enables the formation of discrete NPs without the use of external stabilizers, while simultaneously regulating chain growth, nucleation and particle aggregation, thereby yielding well-defined nanostructures with controlled composition and narrow size distributions.

During copolymer growth, the pronounced contrast in hydrophilicity between polystyrene and sulfonated PAMPS segments promotes compositional self-organization within the developing particles. The hydrophobic polystyrene domains preferentially condense into the particle core, whereas the sulfonated segments migrate toward the particle–solvent interface, resulting in NPs intrinsically enriched with sulfonate groups at the surface. This precipitation-induced segregation generates a core–shell-like architecture featuring a mechanically stable polystyrene interior and a highly charged outer layer. This represents a self-organized surface-functionalized architecture arising intrinsically from

precipitation polymerization, without post-functionalization. The surface localization of $–SO_3^-$ functionalities markedly increases the density and accessibility of ion-exchange sites, reduces diffusional limitations and provides a favorable electrostatic environment for the adsorption of cationic dye molecules. Accordingly, the systematic enhancement in adsorption capacity with increasing PAMPS content directly reflects the progressive enrichment of surface sulfonate groups, confirming the effectiveness of this strategy in coupling NP formation with controlled surface functionalization for high-efficiency cationic dye removal.

3.1. FT-IR Analysis

The chemical structure and successful copolymerization of the PSt/PAMPS nanoparticle series were verified by FT-IR spectroscopy (Figure 2). NP-PSt displayed the characteristic polystyrene signals, including aromatic C–H stretching at 3081–3024 cm^{-1}, aliphatic C–H stretching at 2917 and 2847 cm^{-1}, aromatic ring C=C vibrations at 1601 and 1493 cm^{-1} and monosubstituted benzene out-of-plane C–H bending at 749 and 700 cm^{-1}. In contrast, NP-PAMPS exhibited a broad N–H/O–H stretching band centered at 3458 cm^{-1}, amide I (C=O) stretching at 1644 cm^{-1}, amide II (N–H bending/C–N stretching) at 1482–1451 cm^{-1} and most intense asymmetric O=S=O stretching at 1230 and 1186 cm^{-1} together with symmetric S–O stretching at 1036–1000 cm^{-1}, confirming the sulfonated PAMPS network.

The copolymer spectra (NP-PSt/AMPS-10, -30, and -50) simultaneously displayed features of both parent homopolymers, providing unequivocal evidence of successful copolymerization. The aromatic C–H (3083–3023 cm^{-1}), aliphatic C–H (2914–2849 cm^{-1}), and ring C=C (1601–1493 cm^{-1}) bands of the PSt framework exist in all three compositions. Concurrently, the progressive emergence of the amide I band at 1640–1625 cm^{-1}, the broad N–H/O–H absorption near 3448–3457 cm^{-1}, and the sulfonate stretching vibrations at 1188–1130 cm^{-1} (asymmetric) and 1046–1010 cm^{-1} (symmetric) confirmed the incorporation of PAMPS segments, with the relative intensity of these sulfonate-related bands increasing systematically from NP-PSt/AMPS-10 through NP-PSt/AMPS-50, consistent with the progressive increase in sulfonation degree across the series.

3.2. Thermogravimetric Analysis

The thermal decomposition behavior of the nanoparticle series was characterized by TGA/DTG (Figure 3 and Table 1). NP-PSt underwent a single mass-loss step with a sharp DTG maximum at 423.2 °C, corresponding to main-chain scission and depolymerization, with negligible high-temperature residue characteristic of polystyrene under inert atmosphere. NP-PAMPS illustrated multistep degradation (DTG maxima at ~200.3, 234.6, 256.6, 280.2, and 331.2 °C), signifying sequential dehydration, sulfonate side-group decomposition and backbone cleavage, with appreciable residue derived from thermally stable sulfonated species.

The copolymer thermograms bridge these two extremes. NP-PSt/AMPS-10 introduces a low-temperature DTG peak at ~189.8 °C absent in NP-PSt and attributable to AMPS-derived moieties, alongside a dominant PSt decomposition maximum at 428.2 °C. NP-PSt/AMPS-30 exhibited an intensified early event at ~194.2 °C, a distinct mid-temperature peak at ~328.1 °C, and a principal maximum shifted to 434.6 °C. The progressive amplification of PAMPS-related degradation features and increasing high-temperature residue with rising AMPS content, combined with the co-existence of both PSt- and PAMPS-characteristic thermal events within single thermograms, corroborated the formation of copolymer NPs rather than physical blends.

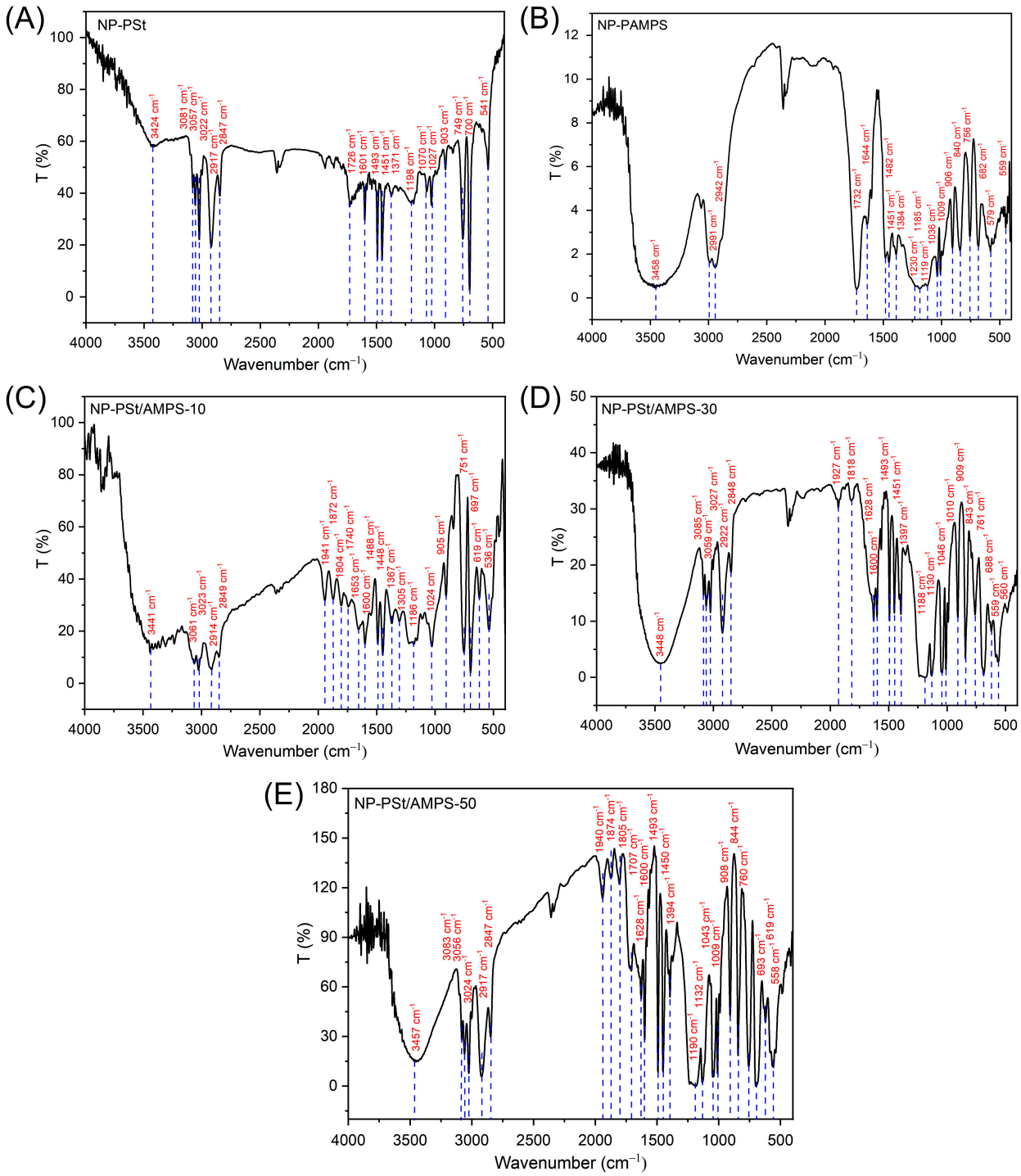

Figure 2. FT−IR spectra of crosslinked polymeric NPs, including (**A**) NP-PSt (pure polystyrene), (**B**) NP-PAMPS (pure poly(2-acrylamido-2-methylpropane sulfonate)), and PSt/PAMPS copolymer NPs with nominal compositions of (**C**) 90:10 (NP-PSt/AMPS-10), (**D**) 70:30 (NP-PSt/AMPS-30), and (**E**) 50:50 (NP-PSt/AMPS-50).

The emergence of a low-temperature DTG maximum near 190–200 °C in both copolymer samples, absent in NP-PSt and characteristic of PAMPS, together with the persistence of the high-temperature PSt decomposition peak at ~423–435 °C, validated the successful integration of sulfonated segments into the PSt network. The progressive rise in low-/mid-temperature events and high-temperature residue with increasing AMPS content further evinced composition-dependent thermal behavior consistent with true copolymer formation.

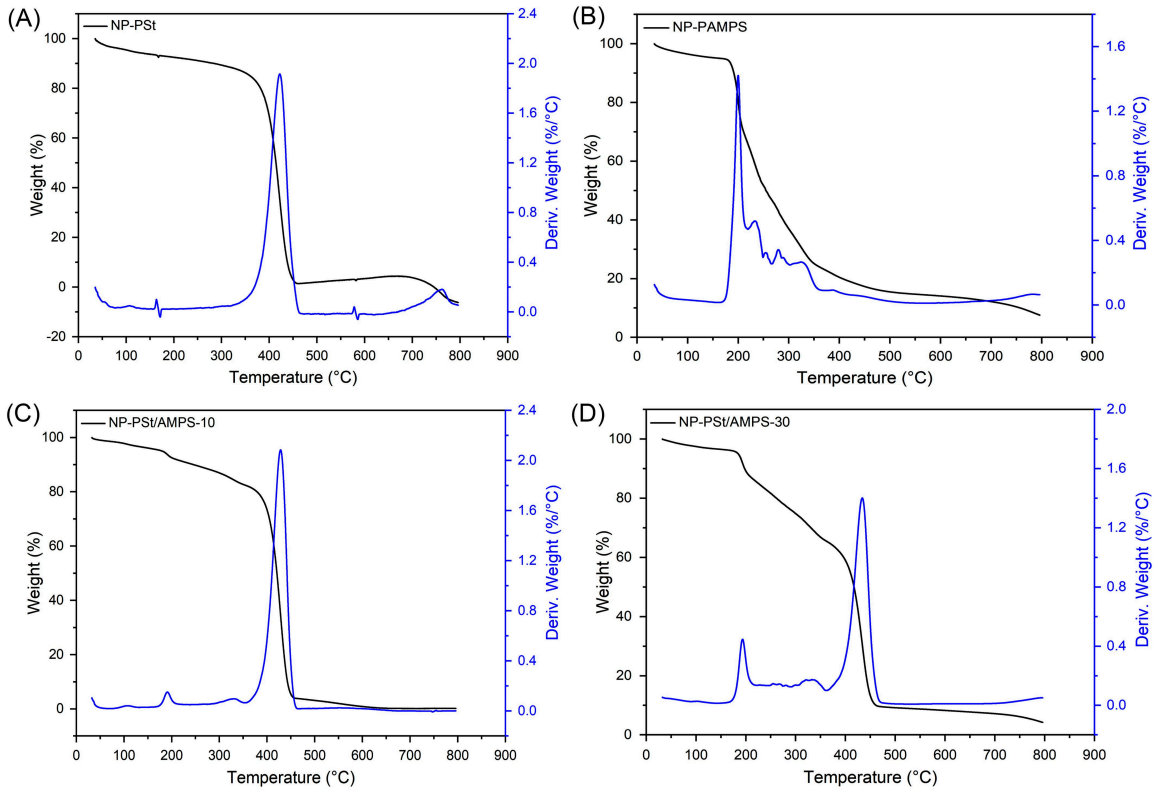

Figure 3. Thermogravimetric (TG) and derivative thermogravimetric (DTG) curves (blue curve) of crosslinked polymeric NPs, including (**A**) NP-PSt (pure polystyrene), (**B**) P-PAMPS (pure poly(2-acrylamido-2-methylpropane sulfonate)), and PSt/PAMPS copolymer NPs with nominal compositions of (**C**) 90:10 (NP-PSt/AMPS-10) and (**D**) 70:30 (NP-PSt/AMPS-30).

Table 1. Thermal decomposition parameters of NP-PSt, NP-PAMPS and PSt/PAMPS copolymer NPs.

Sample	T_{onset} (°C) *	DTG Tmax (°C)	Main Assignment	Residue at High T (Trend)
NP-PSt	~350	423.2	PSt backbone scission/depolymerization	Very low (<1 wt.%)
NP-PAMPS	~180	200.3, 234.6, 256.6, 280.2, and 331.2	Dehydration + sulfonated side-group and backbone degradation	High (≈10–20 wt.%)
NP-PSt/AMPS-10	~200	189.8 and 428.2	AMPS-related early degradation + PSt main-chain scission	Low–moderate
NP-PSt/AMPS-30	~190	194.2, 328.1, and 434.6	AMPS-rich side-group degradation + reinforced PSt backbone scission	Moderate–high

* T_{onset} estimated from the initial deviation of TG curves.

3.3. Morphological Features and Particle Size Distribution

The morphology of the synthesized NPs was inspected by SEM at 5000× and 10,000× magnifications (Figure 4), and particle size distributions were quantitatively estimated. NP-PSt revealed well-defined spherical particles with smooth surfaces and a mean diameter of 715.2 ± 77 nm (Figure 4A–C). Incorporation of 10 wt.% AMPS reduced the mean diameter to 618.4 ± 99 nm and introduced perceptible surface roughening (Figure 4D–F), implying that a modest sulfonate fraction enhanced nucleation density and partially stabilizes growing nuclei through electrostatic repulsion. At 30 wt.% AMPS, the mean diameter further diminished to 469.8 ± 88 nm, with densely packed quasi-spherical particles, showing a no-

tably rougher surface texture (Figure 4G–I). NP-PSt/AMPS-50 markedly differed from the quasi-spherical morphology of the lower-AMPS compositions, exhibiting highly irregular, rough, and extensively aggregated structures, in which individual particle boundaries are no longer clearly resolved with a dimeter of 340 ± 68 nm (Figure 4J–L). This morphological transition is in line with the dominance of the highly hydrophilic PAMPS segments at elevated sulfonation levels, which alters the nucleation growth dynamics during precipitation copolymerization and promotes the formation of interconnected, non-spherical domains. Most importantly, the transition from spherical to irregular morphology at high PAMPS content may increase surface roughness and active site exposure, thereby enhancing adsorption efficiency.

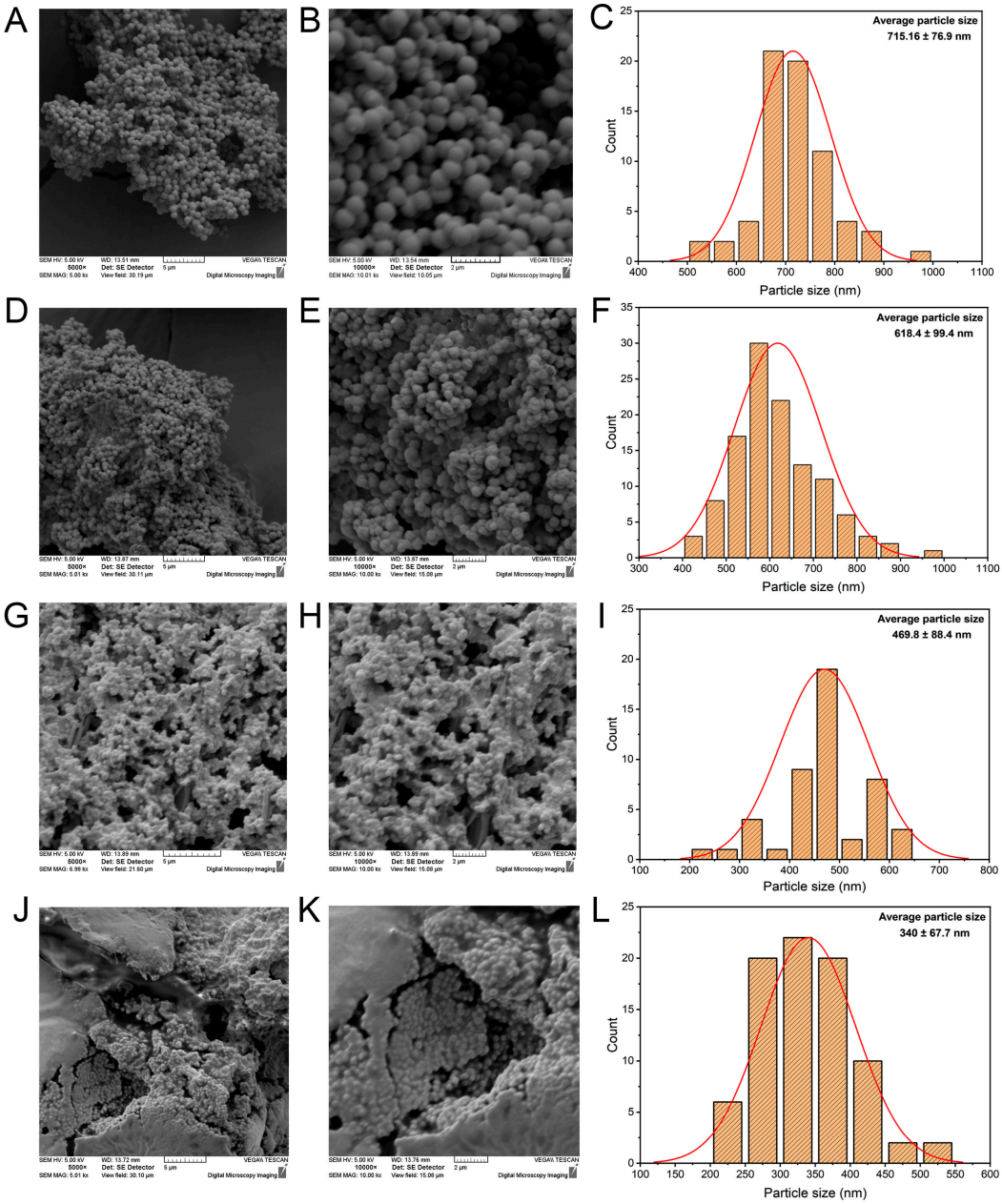

Figure 4. SEM morphology and particle size distributions of PSt/PAMPS NPs. Representative micrographs at 5000× and 10,000× magnifications of (**A**,**B**) NP-PSt, (**D**,**E**) NP-PSt/AMPS-10, (**G**,**H**) NP-PSt/AMPS-30, and (**J**,**K**) NP-PSt/AMPS-50, with corresponding particle size distribution histograms (**C**,**F**,**I**,**L**) following measuring 70–80 NPs. Scale bar = 5 µm for (**A**,**D**,**G**,**J**), whereas scale bar = 2 µm for (**B**,**E**,**H**,**K**).

The monotonic decrease in particle size across the series (NP-PSt > NP-PSt/AMPS-10 > NP-PSt/AMPS-30 > NP-PSt/AMPS-50) and the concurrent evolution from smooth spherical to rough irregular morphologies with increasing AMPS content demonstrated a clear composition-dependent modulation of NP formation. This provides a direct structural basis for the variations in surface charge density, ion-exchange capacity, and adsorption performance that will be outlined in subsequent sections.

3.4. Colloidal Properties and Structure–Property Correlations

Hydrodynamic Size and Surface Charge

The dry-state morphology (SEM) and solution-phase colloidal behavior (DLS, zeta potential) of the PSt/PAMPS nanoparticle series are compared in Table 2. SEM revealed quasi-spherical particles with diameters of 715.2 ± 77 nm, 618.4 ± 99 nm, and 469.8 ± 88 nm for (NP-PSt), (NP-PSt/AMPS-10), and (NP-PSt/AMPS-30), respectively. On the other hand, NP-PSt/AMPS-50 exhibited irregular and aggregated morphological features with a dimeter of 340 ± 68 nm.

Table 2. Colloidal and interfacial properties of NP-PSt, NP-PAMPS and PSt/PAMPS copolymer nanoparticles, including SEM-derived mean diameter, DLS Z-average size, polydispersity index (PDI) and zeta potential.

Sample	SEM Mean Diameter (nm)	DLS Z-Average (nm)	PDI	Zeta Potential (mV)	Colloidal Stability	IEC (meq/g)
NP-PSt	715.2 ± 77	1224	0.120	−36.1	High	0.60 ± 0.20
NP-PSt/AMPS-10	618.4 ± 99	742	0.410	−43.2	Very high	4.27 ± 0.31
NP-PSt/AMPS-30	469.8 ± 88	630	0.622	−41.8	Very high	6.00 ± 0.40
NP-PSt/AMPS-50	340 ± 68 nm	327	0.480	−42.0	Very high	8.47 ± 0.42
NP-PAMPS	(aggregated cores)	511	0.555	−51.0	Excellent	---

The hydrodynamic diameter measured by DLS decreased across the copolymer series from 1224 nm (PDI = 0.120) for NP-PSt to 742 nm (PDI = 0.410), 630 nm (PDI = 0.622), and 326.9 nm (PDI = 0.480) for NP-PSt/AMPS-10, NP-PSt/AMPS-30, and NP-PSt/AMPS-50, respectively, before augmenting to 511 nm (PDI = 0.555) for NP-PAMPS. The rebound in hydrodynamic size for NP-PAMPS, despite possessing the highest sulfonation degree, is consistent with the extensive aggregation observed by SEM for pure PAMPS NPs. The progressive rise in PDI from 0.120 (NP-PSt) to 0.480–0.622 (copolymers) indicates the emergence of bimodal size distributions at higher sulfonation levels. Notably, the DLS profile of NP-PSt/AMPS-50 revealed a dominant population at ~483 nm (93.5% intensity) alongside a minor secondary population at ~4940 nm (6.5%), pointing to the co-existence of primary NPs with larger aggregated domains generated by the enhanced nucleation density of strongly ionic systems.

The increasing discrepancy between dry (SEM) and hydrated (DLS) dimensions with increasing AMPS content across the copolymer series substantiated that the sulfonated segments predominantly regulate the hydrated corona and solvation shell rather than the rigid polymer core. Zeta potential measurements corroborated this compositional trend, with values of −36.1, −43.2, −41.8, −42.0, and −51.0 mV for NP-PSt, NP-PSt/AMPS-10, NP-PSt/AMPS-30, NP-PSt/AMPS-50, and NP-PAMPS, respectively. All values exceed the $|\zeta| > 30$ mV stability threshold, proving robust electrostatic stabilization. The charge plateau observed across the copolymer series (approximately −41.8 to −43.2 mV for 10–50 wt.% AMPS) suggests that the interfacial charge density approaches an effective saturation at moderate sulfonation levels. However, it is worth mentioning that the PDI and DLS size distributions indicated increased aggregation at higher AMPS contents, particularly for NP-PSt/AMPS-50. Such aggregation may reduce the fraction of surface area that

is directly exposed to the continuous phase and may partially mask additional sulfonate groups, thereby contributing to the apparent plateau in zeta potential. The measured values therefore likely reflected a combined effect of high interfacial sulfonation and aggregation-induced shielding of surface charges, rather than surface charge saturation alone. Although direct radial mapping of the chemical composition (e.g., by TEM/EDX line profiles) was not performed in this study, the combination of FT-IR evidence of sulfonate incorporation, the monotonic increase in zeta potential magnitude with AMPS content and the strong sensitivity of adsorption to surface charge is consistent with a model in which PAMPS segments are enriched at the nanoparticle surface while PSt-rich domains form the interior.

To quantify the density of ion-exchange sites, the ion-exchange capacity (IEC) of the nanoparticle series was determined by acid–base back-titration as summarized in Table 2. IEC increased sharply with increasing AMPS content, from 0.60 ± 0.20 meq g^{-1} for the non-sulfonated NP-PSt to 4.27 ± 0.31 meq g^{-1} for NP-PSt/AMPS-10, 6.00 ± 0.4 meq g^{-1} for NP-PSt/AMPS-30 and 8.47 ± 0.42 meq g^{-1} for NP-PSt/AMPS-50, suggesting the progressive amalgamation of PAMPS segments into the crosslinked network. These IEC values fall within the range reported for sulfonated polystyrene and PAMPS-based ion-exchange materials and, together with the increasingly negative zeta potentials, confirm the formation of nanoparticles with a high density of accessible sulfonate groups at intermediate and high AMPS loadings. The composition-dependent IEC trend mirrors the observed hierarchy in adsorption performance (NP-PSt < NP-PSt/AMPS-10 < NP-PSt/AMPS-30 < NP-PSt/AMPS-50), supporting the conclusion that ion-exchange site density is a key determinant of dye uptake in this system.

3.5. Adsorption Process

Following the structural, morphological and colloidal characterization of the PSt/PAMPS nanoparticle series, their adsorption performance toward Crystal Violet (CV) and Methylene Blue (MB) was evaluated under varying conditions, including contact time, temperature, initial dye concentration, solution pH and adsorbent dose. CV and MB were selected as model cationic pollutants due to their contrasting molecular architectures, i.e., a planar phenothiazinium skeleton (MW = 319.85 g mol^{-1}) for MB and a bulkier propeller-shaped triarylmethane framework (MW = 407.99 g mol^{-1}) for CV facilitating an assessment of the role of adsorbate geometry in the uptake behavior.

Across all experiments, a consistent composition-dependent hierarchy was observed: NP-PSt < NP-PSt/AMPS-10 < NP-PSt/AMPS-30 < NP-PSt/AMPS-50, which correlates directly with the progressive increase in sulfonate group density and ion-exchange capacity (IEC). Furthermore, the removal of MB consistently exceeded that of CV under identical conditions, which can be attributed to the compact, planar geometry of MB, allowing superior access to $–SO_3^-$ binding sites in comparison to the sterically demanding CV structure. Throughout the adsorption experiments, the supernatants obtained after centrifugation remained clear, with no detectable increase in baseline absorbance beyond that attributable to the residual dye, and no visible turbidity, suggesting that nanoparticle dissolution or significant polymer leaching was negligible under the tested conditions. This is consistent with the use of MBAA as a crosslinker to form insoluble, networked nanoparticles.

3.5.1. Effect of Contact Time

The time-dependent adsorption profiles of CV and MB on PSt/PAMPS NPs exhibited a characteristic biphasic behavior, consisting of a rapid initial uptake followed by a gradual approach to equilibrium as shown in Figure 5A,B. It is apparent from the data in Figure 5A for MB that the initial adsorption stage is particularly pronounced, with NP-PSt/AMPS-50, achieving approximately 60–65% removal within the first 10–15 min, corresponding to

nearly 90% of its equilibrium capacity (~68–70%). In contrast, the non-sulfonated NP-PSt reached only ~10–15% removal over the same time interval, highlighting the critical role of surface sulfonate groups in governing adsorption kinetics. A similar trend is observed for CV (Figure 5B), albeit with lower overall removal efficiencies, where NP-PSt/AMPS-50 reaches ~45–48% within 10 min and plateaus at ~50–52% at equilibrium. The comparatively slower uptake and reduced capacity for CV can be attributed to its bulkier triarylmethane structure, which imposes steric limitations on diffusion and access to surface-exposed $–SO_3^-$ binding sites, in contrast to the more planar and compact MB molecule.

The initial adsorption rate (h) increased systematically with PAMPS content, following the order: NP-PSt < NP-PSt/AMPS-10 < NP-PSt/AMPS-30 < NP-PSt/AMPS-50, which correlates with the progressive increase in surface charge density and ion-exchange capacity. This rapid initial uptake is primarily governed by electrostatic interactions between cationic dye molecules and the highly accessible sulfonate groups localized at the nanoparticle surface. As adsorption proceeds, the rate gradually decreases due to the progressive occupation of active sites and reduced concentration gradients, with the later stage controlled by intraparticle diffusion and surface-mediated interactions.

Notably, the faster kinetics and higher removal efficiency observed for MB compared to CV across all compositions further confirm that adsorption is not solely governed by electrostatic attraction, but it is also strongly influenced by molecular size, geometry and diffusional accessibility. These results demonstrate that the engineered PSt/PAMPS NPs enable rapid and efficient adsorption through a synergistic combination of high surface charge density and nanoscale accessibility of active sites. These factors collectively facilitate rapid external-surface binding of MB and CV, consistent with the swift uptake reported for CV and chromium (VI) on SPGMA and CV-SPGMA adsorbents [28–30]. As adsorption progresses, the progressive occupation of available binding sites and the depletion of dye in the solution diminish the mass-transfer driving force, resulting in a deceleration of the removal rate. The latter stage (beyond approximately 30 to 45 min) is predominantly regulated by intraparticle diffusion and chemisorption-controlled attachment within the polymer network, As also suggested by the two-stage uptake profiles and the slower late-stage approach to equilibrium, the later part of the process for SPGMA-based adsorbents is likely influenced by intraparticle diffusion and surface-mediated interactions [29,30]. This two-stage kinetic pattern, characterized by a rapid initial uptake followed by a gradual approach to equilibrium, is consistent with previous reports on sulfonated polymeric adsorbents such as SPGMA and CV-SPGMA utilized for the removal of CV and chromium(VI) [28–30]. The rapid initial uptake and relatively short time to equilibrium observed for NP-PSt/AMPS-50, particularly for MB (~60–70% removal within 10–15 min and equilibrium within 100–120 min), indicated that adsorption is ruled by interactions at readily accessible surface-localized sulfonate sites, rather than by slow intraparticle diffusion through a thick hydrogel matrix. This kinetic behavior contrasts with many AMPS-based bulk hydrogels and cryogels, where internal diffusion often governs the late-stage uptake, especially at high dye loadings, despite their high overall water content. The precipitation-induced core–shell-like organization of PSt/PAMPS nanoparticles therefore provides a complementary design paradigm to conventional AMPS networks, emphasizing nanostructured, surface-enriched architectures to maximize active-site accessibility and accelerate ion-exchange-driven adsorption [18,31–33].

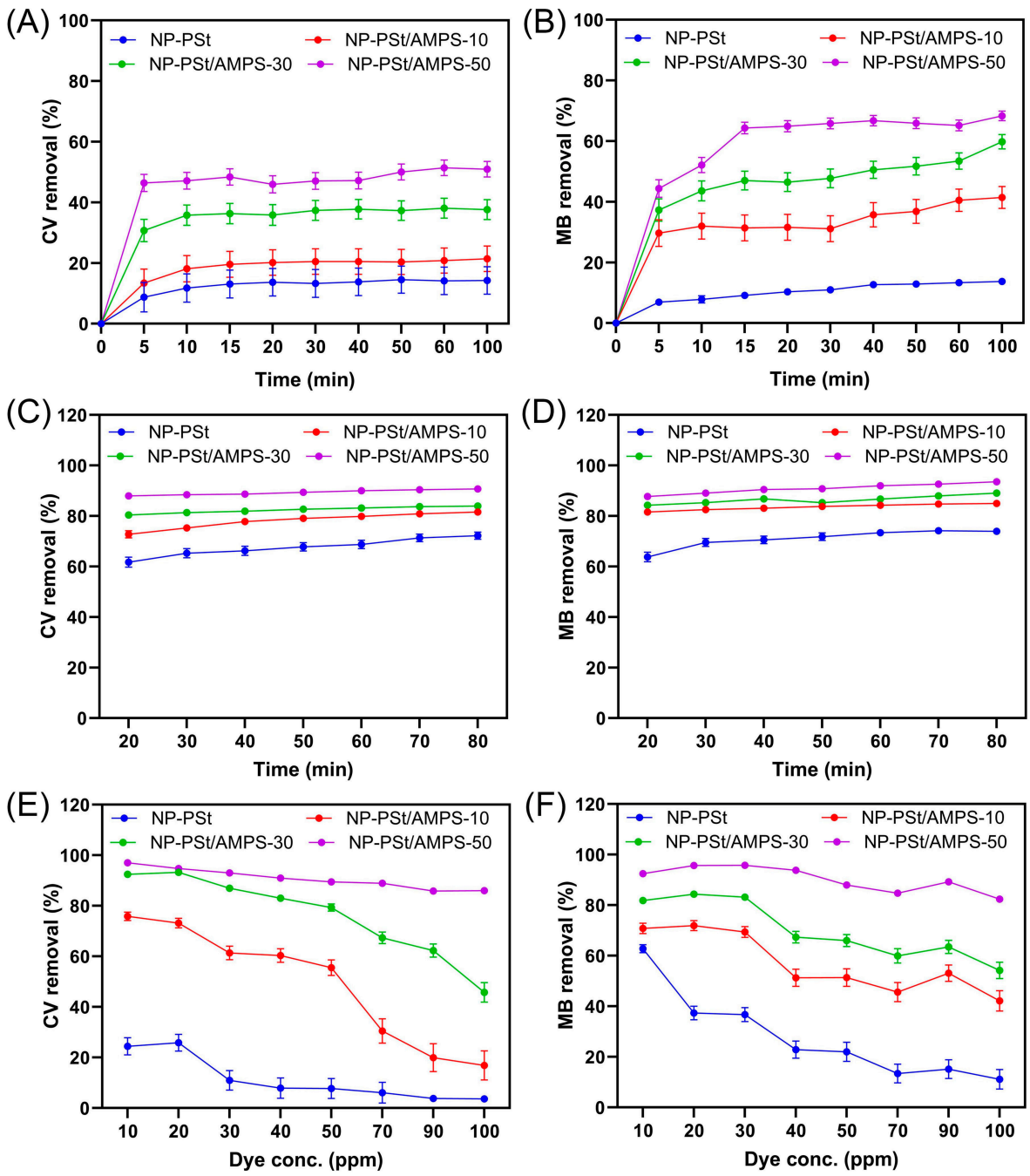

Figure 5. Effect of (**A**,**B**) contact time from (0–100 min), (**C**,**D**) adsorption temperature (20–80 °C), and (**E**,**F**) initial dye concentration (10–100 ppm) on the removal efficiency (%) of crystal violet (CV) and methylene blue (MB) by PSt/PAMPS NPs. A consistent composition-dependent trend of NP-PSt < NP-PSt/AMPS-10 < NP-PSt/AMPS-30 < NP-PSt/AMPS-50 was observed across all conditions for both dyes, correlating with the increase in sulfonate group density and ion-exchange capacity. All parameters were assessed in triplicate, and data are shown as mean ± SD.

3.5.2. Effect of Temperature

The impact of temperature on the removal efficiencies of CV and MB within the range of 20–80 °C is illustrated in Figure 5C,D. Across all NP-PSt/AMPS formulations, a progressive increase in removal efficiency was observed with rising temperature, thereby confirming the endothermic nature of the adsorption process. This indicates that adsorption is not governed solely by diffusion, but involves thermally activated interactions at the polymer–solution interface, consistent with an activation-controlled ion-exchange

mechanism. Specifically, for MB, the NP-PSt/AMPS-50 formulation exhibited an increase in removal efficiency from approximately 80% at 20 °C to approximately 89% at 80 °C. In contrast, NP-PSt demonstrated a more pronounced enhancement, rising from approximately 40% to approximately 57% over the same temperature interval. A comparable trend was perceived for CV, wherein NP-PSt/AMPS-50 increased from approximately 80% to approximately 85%, while NP-PSt progressed from approximately form 37% to approximately 54% between 20 °C and 80 °C.

The temperature-induced enhancement in uptake can be elucidated through several cooperative mechanisms. Firstly, elevated temperatures augment the thermal mobility of CV and MB molecules, as well as the frequency of effective collisions with the sulfonated nanoparticle surface, thereby facilitating the overcoming of activation barriers associated with chemisorption. Secondly, thermal treatment is anticipated to promote partial swelling of the AMPS-rich polymer domains, thereby exposing additional sulfonate sites that are less accessible at lower temperatures. Thirdly, the diminution in solution viscosity with increasing temperature enhances external film mass transfer and intraparticle diffusion, which aligns with the broader literature regarding the endothermic uptake of dyes and oxyanions onto sulfonated polymeric nano-adsorbents, consistent with the general picture of endothermic uptake of dyes on sulfonated polymeric hydrogels and nanocomposites reported elsewhere [34–36].

Furthermore, the magnitude of the temperature effect diminished as the AMPS content increases. NP-PSt, characterized by the lowest density of sulfonate groups, exhibited the largest absolute gains (approximately 17% for MB and approximately 17–18% for CV), whereas NP-PSt/AMPS-50 showed more modest increases between 20 °C and 80 °C of approximately 9% and 5% for MB and CV, respectively. For NP-PSt/AMPS-50, the relatively modest increase in removal efficiency with temperature is consistent with a system in which most accessible sulfonate sites are already effectively utilized at ambient conditions. Therefore, additional thermal activation only slightly enhanced uptake. By contrast, NP-PSt, which contains very few sulfonate groups, exhibited a more pronounced temperature sensitivity. This behavior is attributed to temperature-induced improvements in diffusion and mass transfer within the hydrophobic polymer matrix, and to increased mobility of the polymer chains, rather than to any saturation of electrostatic binding sites. At higher temperatures, enhanced segmental dynamics and reduced solution viscosity can facilitate deeper penetration of dye molecules into the particle and better utilization of otherwise poorly accessible regions.

3.5.3. Effect of Initial Dye Concentration

The influence of initial dye concentration on the removal efficiency of crystal violet (CV) and methylene blue (MB) is depicted in Figure 5E,F. For all PSt/PAMPS formulations, a clear inverse relationship between removal efficiency and initial dye concentration was reported, particularly at higher concentrations (≥40–50 ppm). For MB (Figure 5E), NP-PSt/AMPS-50 maintained high removal efficiency (~92–96%) at low concentrations (10–30 ppm), followed by a gradual decline to ~82–85% at 100 ppm. Conversely, samples with lower sulfonation, such as NP-PSt/AMPS-10 and NP-PSt, exhibited a pronounced decrease, reaching ~42% and ~10–12%, respectively, at 100 ppm.

A similar trend was perceived for CV (Figure 5F), showing that NP-PSt/AMPS-50 retained high performance (~85–90%) across the concentration range, while NP-PSt/AMPS-30 and NP-PSt/AMPS-10 markedly decreased to ~45% and ~15–20%, respectively, at 100 ppm. The stronger sensitivity of CV adsorption to concentration is attributed to its larger molecular size and steric hindrance, which limits diffusion and accelerate the effective saturation of surface-accessible binding sites compared with the more compact MB

molecules. The equilibrium capacities calculated from the batch adsorption data further corroborate these trends. For MB, NP-PSt/AMPS-50 shows qe values increasing from 9.25 mg g^{-1} at 10 mg L^{-1} to 82.44 mg g^{-1} at 100 mg L^{-1}, while the corresponding CV capacities rise from 9.71 to 86.00 mg g^{-1} over the same concentration range. NP-PSt/AMPS-30 also achieves substantial capacities at 100 mg L^{-1} (54.25 mg g^{-1} for MB and 45.81 mg g^{-1} for CV), whereas the non-sulfonated NP-PSt remains below approximately 14 mg g^{-1} for both dyes across all tested concentrations. Overall, these qe values are comparable to or higher than those reported for several AMPS/PAMPS-based hydrogel adsorbents at similar initial dye concentrations, but are attained here with markedly shorter equilibrium times, underscoring the advantage of the nanoscale, surface-sulfonated PSt/PAMPS architecture.

This behavior can be justified by a site-availability and saturation mechanism. At low dye concentrations, the ratio of available sulfonate binding sites to dye molecules is high, facilitating efficient adsorption via electrostatic interactions and ion exchange. As the initial concentration increases, the number of dye molecules exceeds the available active sites on the nanoparticle surface, leading to progressive occupation and eventual saturation. Consequently, a greater fraction of dye remains in solution, resulting in reduced removal efficiency.

Importantly, the reduced sensitivity of NP-PSt/AMPS-50 to concentration changes indicated that higher sulfonation levels provide a greater density of accessible $–SO_3^-$ groups, delaying saturation and maintaining high adsorption performance under elevated pollutant loads. This concentration-dependent behavior is consistent with adsorption on finite active sites, as described by Langmuir-type systems. Specifically, increasing initial concentration enhances adsorption capacity (q_e) while decreasing percentage removal as surface coverage approaches monolayer saturation [34,37,38]. Similar trends were reported for sulfonated polymeric adsorbents, including SPGMA-based systems, where adsorption efficiency is governed by the balance between dye concentration and accessible ion-exchange sites [29,30].

3.5.4. Effect of Solution pH

The influence of solution pH on the removal efficiency of CV and MB is presented in Figure 6A,B. For all sulfonated PSt/PAMPS NPs, the removal efficiency showed a clear and systematic amplification with increasing pH from 4 to 10. In contrast, the non-sulfonated NP-PSt showed minor variations, maintaining relatively constant removal efficiencies (~50–55%) across the examined pH range, indicating limited pH sensitivity in the absence of ionizable functional groups. For MB (Figure 6A), NP-PSt/AMPS-50 demonstrated an increase in removal efficiency from ~78% at pH 4 to ~93% at pH 10, while NP-PSt/AMPS-30 and NP-PSt/AMPS-10 revealed similar trends with lower absolute values. A comparable behavior was detectable for CV (Figure 6B), revealing that removal efficiency increased from ~77% to ~95% for NP-PSt/AMPS-50 over the same pH range. This consistent enhancement substantiated that adsorption is strongly governed by electrostatic interactions between negatively charged sulfonate groups and cationic dye molecules.

The observed pH dependence can be explained based on surface charge evolution and competitive adsorption effects. Under acidic conditions (pH 4–5), the high concentration of H^+ ions compete with MB^+ and CV^+ for $–SO_3^-$ binding sites, leading to partial suppression of dye adsorption. In addition, proton accumulation near the nanoparticle surface compresses the electrical double layer and reduces the effective surface charge, thereby weakening electrostatic attraction. Similar competitive protonation effects have been widely reported for AMPS-based and sulfonated polymer adsorbents [17,34,39]. As the pH increases, the concentration of competing protons decreases, allowing the sulfonate groups to remain fully deprotonated and electrostatically active, which enhances dye adsorption.

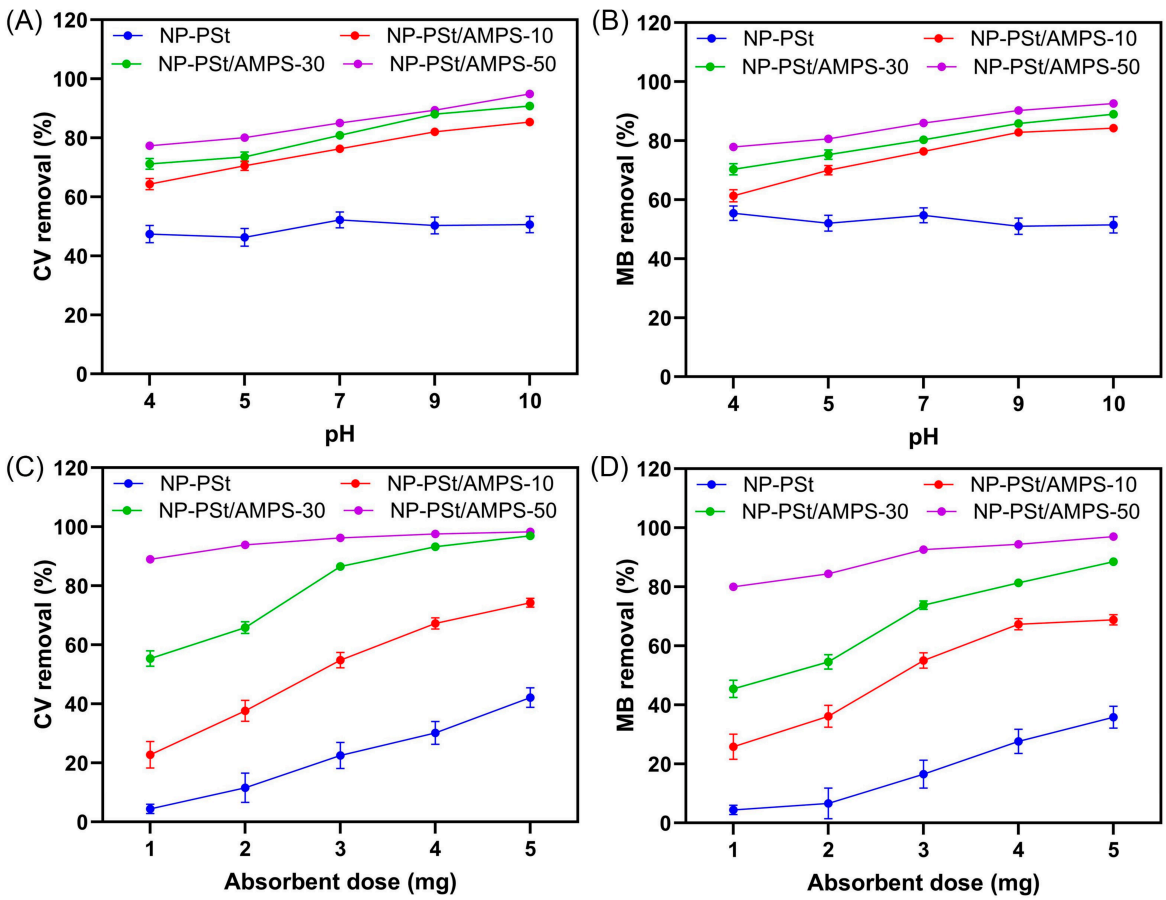

Figure 6. Effect of (**A**,**B**) solution pH (4–10), and (**C**,**D**) adsorbent dose (1–5 mg) on the removal efficiency (%) of crystal violet (CV) and methylene blue (MB) by PSt/PAMPS NPs. A consistent composition-dependent trend (NP-PSt < NP-PSt/AMPS-10 < NP-PSt/AMPS-30 < NP-PSt/AMPS-50) was observed under all conditions for both dyes, corresponding to the progressive increase in sulfonate group density and ion-exchange capacity. All parameters were evaluated in triplicate, and data are shown as mean ± SD.

From a surface chemistry perspective, the investigated pH range is expected to lie above the point of zero charge (pzc) of sulfonated NPs, which typically resides in the acidic region for strongly anionic groups such as $–SO_3^-$. Consequently, the nanoparticle surface remains predominantly negatively charged across the entire pH range, with increasing effective charge density at higher pH values, consistent with zeta potential measurements. This explains the progressive improvement in adsorption efficiency with increasing pH. Importantly, the negligible pH dependence observed for NP-PSt confirms that adsorption is governed primarily by sulfonate functionalities rather than non-specific interactions. The stronger pH responsiveness of highly sulfonated samples (NP-PSt/AMPS-50) highlights the critical role of surface charge density in controlling adsorption performance. These findings demonstrate that adsorption is dominated by charge-regulated ion-exchange interactions, governed by the interplay between solution pH, surface charge evolution, and competitive ion effects. This behaviour reflects the combined influence of proton competition, dye speciation, and the ionization state of the sulfonate groups at the nanoparticle surface. Although the pH-dependent adsorption profiles (Figure 6) clearly indicate that MB and CV uptake are sensitive to solution pH, zeta potential measurements in this work were intentionally conducted at pH 6.5 to characterize the surface charge under the near-neutral conditions most relevant to the kinetic and isotherm studies. A more detailed mapping of the pH dependence of zeta potential (e.g., at pH 4, 7 and 10) would further clarify the

relationship between interfacial charge, dye speciation and adsorption efficiency, and is the focus of ongoing work.

3.5.5. Effect of Adsorbent Dose

The influence of adsorbent dose on the removal efficiency of the 2 dyes is presented in Figure 6C,D. For all PSt/PAMPS formulations, a pronounced increase in removal efficiency was discerned with increasing adsorbent dose from 1 to 5 mg at a fixed dye concentration of 50 ppm. This trend is consistent for both MB (Figure 6C) and CV (Figure 6D), suggesting a direct relationship between adsorbent dosage and the total number of available active sites. For MB, NP-PSt/AMPS-50 exhibited a high removal efficiency of ~80% at a dose of 1 mg, which increased to ~97–98% at 5 mg. Similarly, NP-PSt/AMPS-30 showed a substantial increase from ~45% to ~90%, while NP-PSt/AMPS-10 improved from ~25% to ~68–70% over the same dosage range. In contrast, the non-sulfonated NP-PSt displayed significantly lower performance, reaching only ~35–40% removal at 5 mg, confirming the critical role of sulfonate functionalities in adsorption.

A comparable trend is observed for CV, where NP-PSt/AMPS-50 achieved near-complete removal (~98–100%) at higher doses, while NP-PSt/AMPS-30 and NP-PSt/AMPS-10 reach ~96% and ~74%, respectively, at 5 mg. The progressive enhancement in removal efficiency with increasing dose is attributed to the increase in total surface area and the number of accessible $–SO_3^-$ binding sites, which facilitates stronger electrostatic interactions and ion-exchange capacity for dye molecules. However, the rate of increase in removal efficiency diminishes at higher adsorbent doses, particularly for highly sulfonated samples such as NP-PSt/AMPS-50. This behavior indicates a transition from an adsorbent-limited regime at low doses. Precisely, adsorption is governed by the number of available active sites to an adsorbent-limited regime at higher doses, where the available dye molecules become insufficient to occupy all binding sites. Similar dose-dependent transitions were widely reported for sulfonated polymeric adsorbents and AMPS-based systems [17,34,39].

From a mechanistic perspective, although removal efficiency increases with adsorbent dose, the adsorption capacity per unit mass (q_e) is expected to decrease at higher dosages due to underutilization of active sites and possible particle aggregation effects. This phenomenon is characteristic of adsorption systems governed by finite site availability and has been extensively documented in dye adsorption studies. Overall, the results demonstrate that adsorption performance is strongly dependent on adsorbent dose, with an optimal range of 3–5 mg achieving high removal efficiency while maintaining effective utilization of active sites. The superior performance of NP-PSt/AMPS-50 across all dosages further confirms that adsorption is primarily governed by surface charge density and ion-exchange capacity, reinforcing the proposed structure–charge–function relationship.

3.5.6. Post-Adsorption Characterization

To validate the adsorption data and elucidate the dye-adsorbent interactions at molecular and morphological levels, the PSt/PAMPS NPs were characterized through visual inspection, SEM, and FT-IR spectroscopy both prior to and following exposure to CV and MB solutions. The results are presented in Figures 7 and 8. Visual inspection of the recovered NPs confirmed successful dye uptake across all compositions. The initially white or pale powders exhibited distinct blue and violet coloration, with color intensity corresponding to the AMPS content, thereby aligning with the quantitative removal trends established in preceding sections.

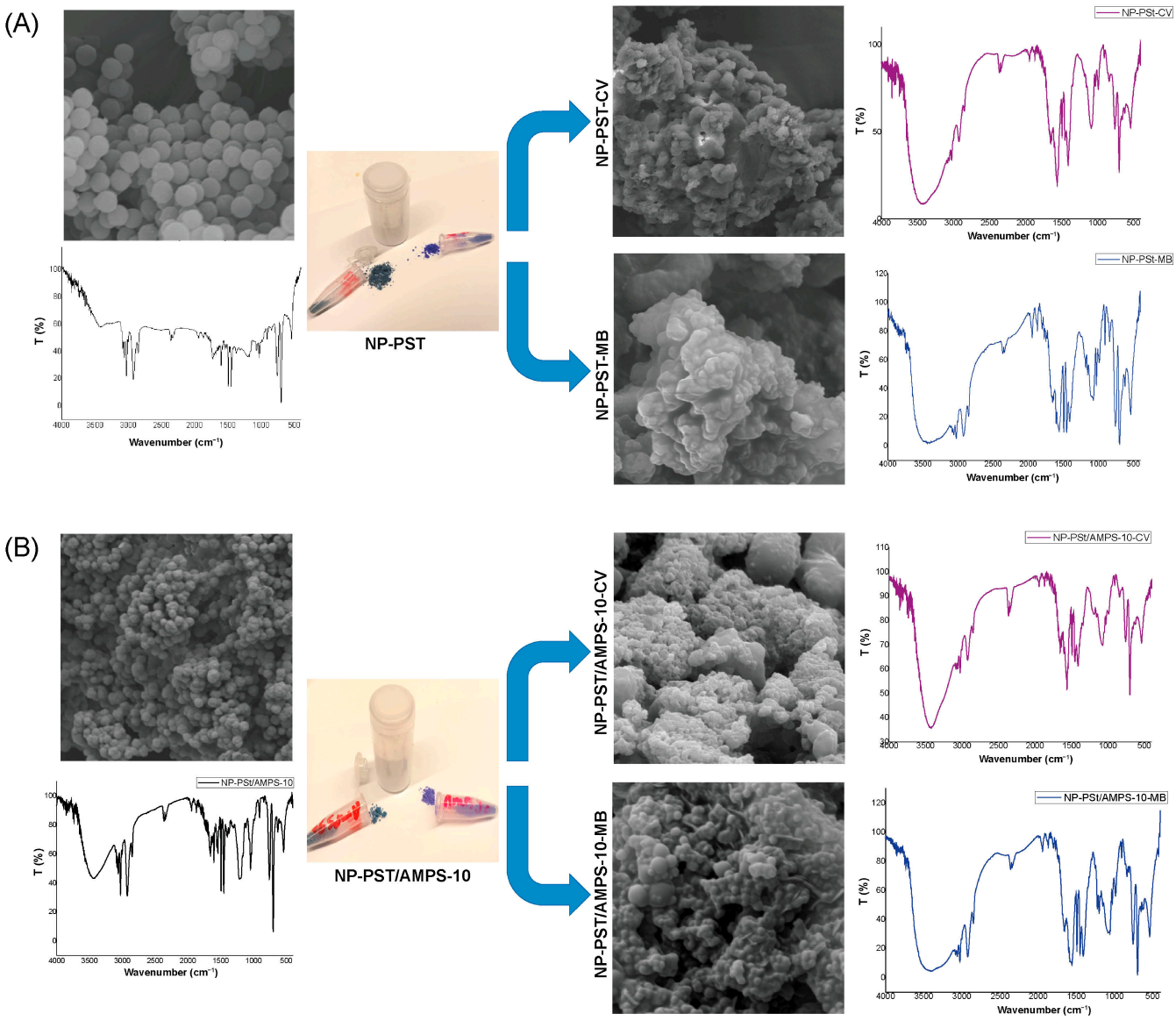

Figure 7. Visual photographs, SEM micrographs, and FT-IR spectra of (**A**) NP-PSt and (**B**) NP-PSt/AMPS-10 before adsorption (left panel) and after adsorption (right panel) of crystal violet (CV) and methylene blue (MB). NP-PSt-CV and NP-PSt-MB denote the NP-PSt NPs post adsorption of CV and MB, respectively, while NP-PSt/AMPS-10-CV and NP-PSt/AMPS-10-MB point to the NP-PSt/AMPS-10 NPs after adsorption of CV and MB, respectively.

SEM micrographs of the pristine NPs demonstrated the well-defined quasi-spherical morphology characteristic of each composition. As previously mentioned, NP-PSt exhibited smooth, uniform surfaces, whereas the sulfonated variants displayed progressively rougher textures with increasing AMPS content. Following dye adsorption, all compositions exhibited significant morphological alterations: The originally discrete nanoparticle surfaces became markedly rougher and more agglomerated, with a partial loss of individual particle definition. These modifications are indicative of dye molecule deposition on the surfaces of the NPs and within their hydrated corona, accompanied by inter-particle bridging mediated by the adsorbed dye species. The morphological disruption was particularly pronounced in the higher-sulfonation samples (NP-PSt/AMPS-30 and NP-PSt/AMPS-50), which is consistent with their enhanced dye loading capacity.

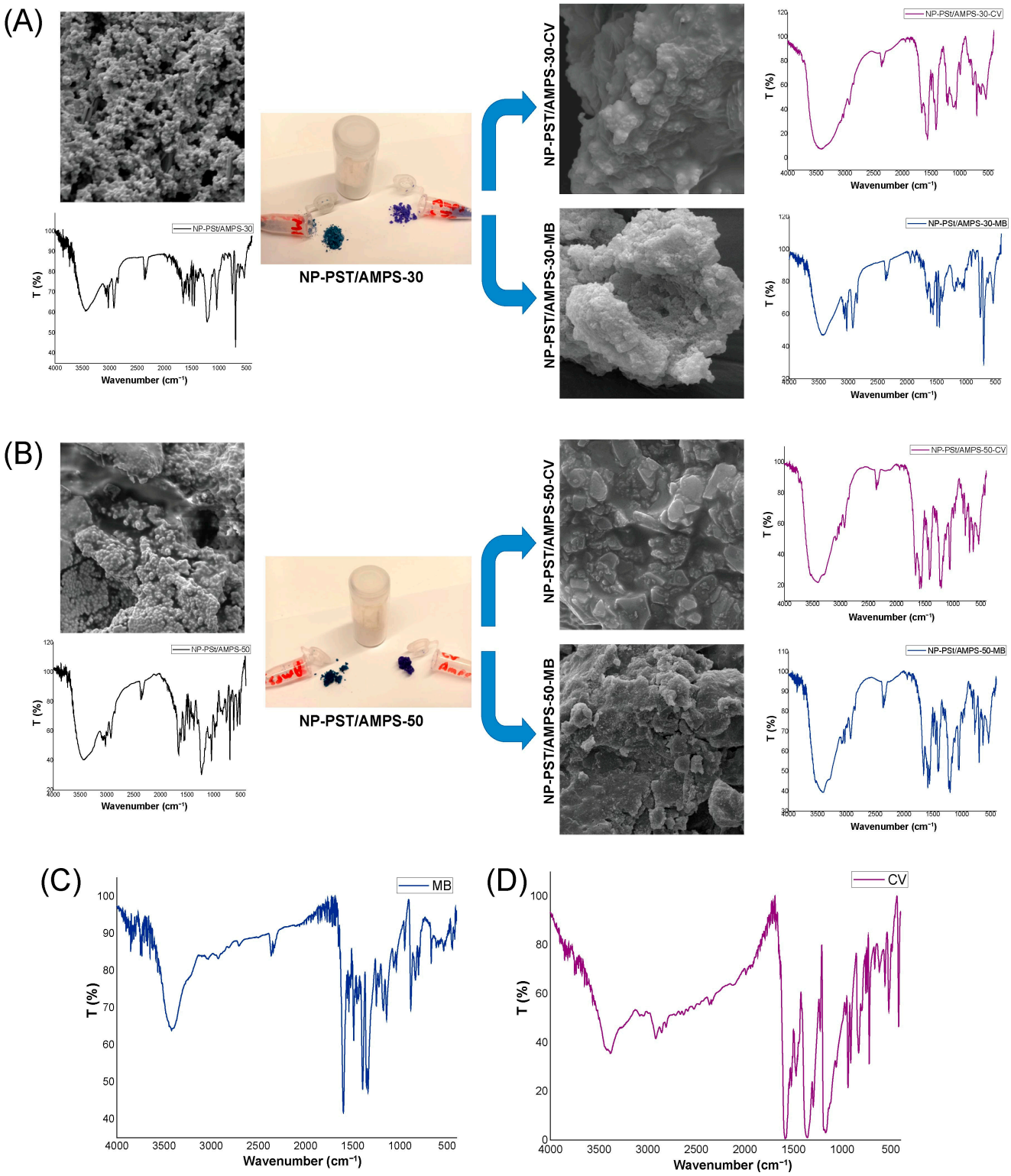

Figure 8. Visual photographs, SEM micrographs, and FT-IR spectra of (**A**) NP-PSt/AMPS-30 and (**B**) NP-PSt/AMPS-50 before adsorption (left panel) and after adsorption (right panel) of crystal violet (CV) and methylene blue (MB). (**C**,**D**) FT-IR spectra of MB and CV, respectively. NP-PSt/AMPS-30-CV and NP-PSt/AMPS-30-MB denote the NP-PSt/AMPS-30 NPs post adsorption of CV and MB, respectively, while NP-PSt/AMPS-50-CV and NP-PSt/AMPS-50-MB point to the NP-PSt/AMPS-50 NPs after adsorption of CV and MB, respectively.

FT-IR analysis provided spectroscopic confirmation of dye–adsorbent interactions. The spectra of the dye-loaded NPs preserved the characteristic absorption peaks of the pristine

PSt/PAMPS framework, signifying that the polymeric backbone remained structurally intact after adsorption. In addition to these features, new absorption bands (at 1600, 1490 and 1400 cm^{-1} for MB; and 1581, 1364, and 1174 cm^{-1} for CV) corresponding to the adsorbed dye molecules were observed. In the MB-loaded samples, additional bands associated with the aromatic C=C and C=N stretching vibrations of the phenothiazinium ring appeared, while the CV-loaded samples exhibited features related to the triarylmethane C=C skeletal vibrations. Furthermore, perturbations in the sulfonate-related bands ($–SO_3^-$ symmetric and asymmetric stretching) were evident across all sulfonated compositions following dye loading, confirming direct electrostatic interactions between the cationic dye molecules and the anionic sulfonate sites. These spectroscopic observations substantiate the electrostatic and ion-exchange adsorption mechanisms proposed throughout this section.

3.6. Reusability and Regeneration Performance

The reusability of the PSt/PAMPS nanoparticles was evaluated over five consecutive adsorption–desorption cycles with MB and CV, as shown in Figure 9. In all cases, the composition-dependent trend observed in single-use experiments (NP-PSt < NP-PSt/AMPS-10 < NP-PSt/AMPS-30 < NP-PSt/AMPS-50) was preserved, indicating that increasing AMPS content enhances both initial adsorption efficiency and retention of performance upon reuse.

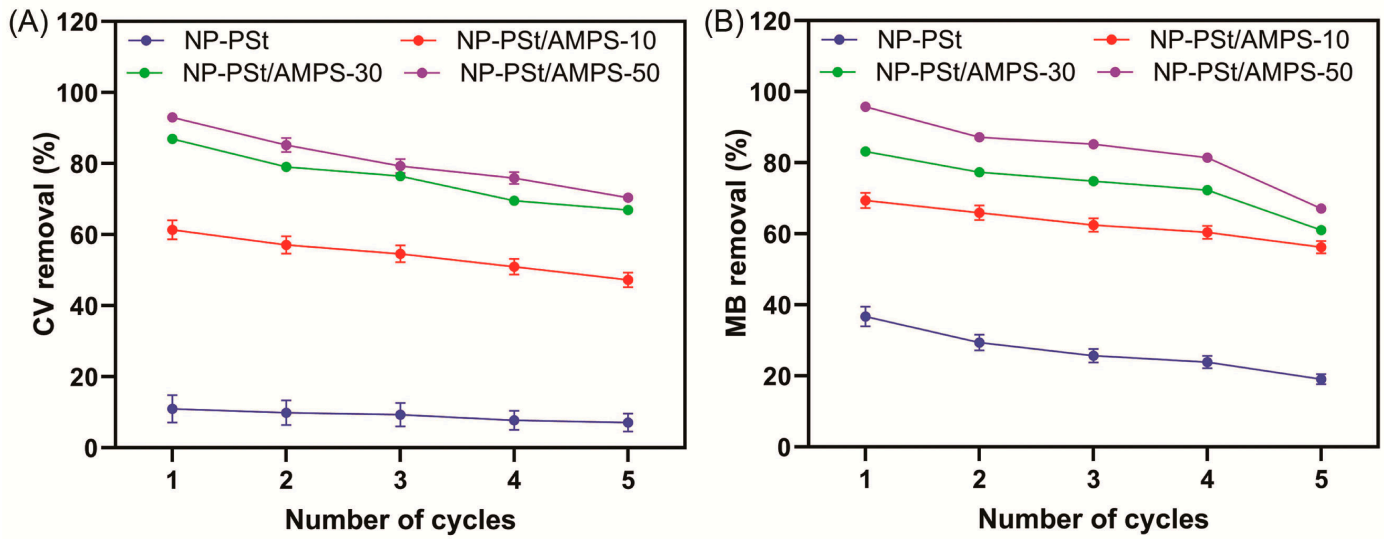

Figure 9. Reusability of PSt/PAMPS nanoparticles for (**A**) CV and (**B**) MB removal over five consecutive adsorptions–desorption cycles. All determinations were conducted in triplicate, and data are shown as mean ± SD.

For MB, NP-PSt/AMPS-50 showed the highest first-cycle removal (95.80%) and still achieved 67.13% in the fifth cycle, while NP-PSt/AMPS-30 decreased from 83.16% to 61.10% and NP-PSt/AMPS-10 from 69.42% to 56.23%. In contrast, NP-PSt dropped from 36.73% to 19.10%, underscoring the importance of sulfonate groups for durable adsorption. A similar pattern was obtained for CV: NP-PSt/AMPS-50 declined from 93.01% to 70.43%, NP-PSt/AMPS-30 from 86.93% to 66.94%, and NP-PSt/AMPS-10 from 61.39% to 47.27%, whereas NP-PSt remained poorly active (11.02% to 7.16%).

Despite gradual efficiency losses, the sulfonated copolymers retained a substantial fraction of their initial activity after five cycles, with MB retention of roughly 81% (NP-PSt/AMPS-10) and 73–70% (NP-PSt/AMPS-30 and NP-PSt/AMPS-50), and similar 75–77% ranges for CV in the highly sulfonated samples. This behavior suggests that AMPS incorporation provides a high density of accessible anionic sites that can withstand repeated

regeneration, while the observed decline is likely due to incomplete desorption of strongly bound dye and minor aggregation or restructuring during cycling. The consistently higher removals for MB than for CV across all cycles further support the role of molecular size and geometry in accessing surface-exposed sulfonate sites. Overall, NP-PSt/AMPS-30 and NP-PSt/AMPS-50 emerged as promising regenerable adsorbents, combining high capacity with robust multi-cycle reuse.

3.7. Adsorption Mechanism

The adsorption of CV and MB onto PSt/PAMPS NPs is governed primarily by electrostatic attraction and ion-exchange between the negatively charged sulfonate groups ($–SO_3^-$) and the cationic dye species (MB^+ and CV^+), with additional contributions from hydrophobic and π–π interactions at the polystyrene domains. The dominant role of charge-regulated adsorption is supported by the systematic increase in dye removal with PAMPS content, the corresponding rise in surface charge density (ζ from −36.1 to −51.0 mV), and the higher ion-exchange capacity of highly sulfonated formulations. The pH-dependent behavior, where adsorption improves at higher pH due to reduced proton competition and increased availability of deprotonated sulfonate sites, further corroborates this electrostatic/ion-exchange mechanism.

Kinetically, the process follows a two-stage pathway: a rapid initial uptake, driven by the high density of readily accessible surface sulfonate groups and strong electrostatic attraction, followed by a slower stage controlled by intraparticle diffusion and progressive site occupation. The gradual approach to equilibrium and the reduced rate at longer contact times or higher dye concentrations are consistent with a finite number of active sites and a transition toward adsorption equilibrium. Within this framework, hydrophobic contacts and possible π–π interactions between the dye aromatic rings and polystyrene phenyl groups may enhance the overall affinity, but they are regarded as secondary to the electrostatic ion-exchange process.

Morphological and spectroscopic analyses support this mechanistic picture. SEM images after adsorption reveal increased surface roughness and aggregation, indicative of dye deposition and possible interparticle bridging. FT-IR spectra of dye-loaded NPs show the appearance of characteristic dye bands together with perturbations in sulfonate stretching vibrations, confirming direct interactions between $–SO_3^-$ groups and cationic dye molecules. Although the FT-IR perturbations of aromatic and sulfonate bands are compatible with contributions from π–π and hydrophobic interactions at the PSt domains, they do not provide direct proof of π–π stacking; this contribution is therefore proposed as a plausible secondary interaction alongside the dominant electrostatic ion-exchange.

The consistently lower adsorption efficiency and slower kinetics observed for CV compared to MB can be rationalized by a combination of steric and molecular factors. CV is a bulkier triarylmethane dye with a higher molecular weight (407.99 g/mol) and a more extended aromatic framework than MB, which implies larger effective molecular dimensions and a different charge distribution at the solid–liquid interface; together, these features are expected to hinder diffusion into confined regions and reduce the packing efficiency of CV at the nanoparticle surface, even under otherwise similar electrostatic driving forces.

Finally, the nanoscale architecture of the PSt/PAMPS system plays a central role in enabling this mechanism. A self-organized core–shell-like structure, with a hydrophobic PSt-rich interior and a sulfonate-rich surface, maximizes exposure of active sites and minimizes diffusion limitations, while the reduction in particle size and increase in surface roughness at higher PAMPS contents further enhance accessibility and adsorption efficiency.

Overall, the adsorption mechanism can thus be described as a charge-regulated ion-exchange process dominated by electrostatic interactions, supplemented by secondary

hydrophobic and π–π contributions and governed by nanoscale structural accessibility. This integrated view explains the observed composition-dependent hierarchy in adsorption performance and underscores the importance of coupling surface-charge engineering with nanostructural design in the development of high-efficiency polymeric nano-adsorbents. It should be noted that all adsorption experiments in this study were performed in single-solute model solutions of MB or CV in water, without additional background electrolytes or organic contaminants. In real dye wastewaters, the presence of inorganic salts, pH-adjusting agents, and other organic species may influence adsorption by screening electrostatic interactions, competing for sulfonate sites, or altering dye speciation. Based on the charge-regulated ion-exchange mechanism established here, high ionic strength and competing cations would be expected to reduce the effective affinity of MB^+ and CV^+ for surface $–SO_3^-$ groups, whereas moderate pH adjustments that maintain sulfonate deprotonation should preserve high uptake. A systematic evaluation of these matrix effects using representative industrial effluents will be an important focus of future work to fully assess the robustness of PSt/PAMPS nanoparticles under realistic conditions.

4. Conclusions

In this work, composition-controlled sulfonated polymeric nanoparticles based on polystyrene and poly(2-acrylamido-2-methyl-1-propanesulfonic acid) were synthesized via a surfactant-free precipitation polymerization route that intrinsically generates a core–shell-like architecture with a hydrophobic PSt core and a sulfonate-enriched surface. Comprehensive chemical, thermal, morphological and colloidal characterization verified the copolymer formation and revealed a systematic reduction in particle size, enhanced surface charge density and increased ion-exchange capacity with rising PAMPS content, establishing a clear structure–charge–function relationship. Adsorption studies using methylene blue and crystal violet demonstrated that the highly sulfonated nanoparticles achieve rapid uptake, high removal efficiencies at low and high dye concentrations and robust performance over a broad range of solution conditions, consistently surpassing the non-sulfonated counterpart. The superior removal of methylene blue compared to crystal violet highlights the additional role of molecular size and geometry in accessing surface-exposed sulfonate sites. Mechanistically, the results support a synergistic contribution of electrostatic attraction, ion exchange, and π–π interactions, all facilitated by the nanoscale localization and high accessibility of $–SO_3^-$ groups at the particle water interface.

Altogether, this study demonstrates that surfactant-free precipitation copolymerization of PSt/PAMPS offers a scalable platform for the rational design of charge-regulated polymeric nano adsorbents. The quantitative link between copolymer composition, interfacial charge and macroscopic adsorption performance provides a mechanistic blueprint for developing next-generation sustainable sorbents for cationic dye removal and, more broadly, other positively charged pollutants in wastewater. Future work integrating full kinetic/thermodynamic modeling and regeneration/reusability studies will further consolidate the technological relevance of these systems for sustainable water purification.

Author Contributions: T.M.T.: Conceptualization, Data curation, Formal analysis, Investigation, Methodology, Project administration, Validation, Writing—original draft, Writing—reviewing & editing. M.A.H.: Formal analysis, Visualization, Writing—original draft, Writing—reviewing & editing. T.K.-C.: Project administration, Formal analysis, Investigation, Methodology, Validation, Writing—original draft. M.S.M.: Formal analysis, Writing—reviewing & editing. I.P.: Project administration, Validation, Writing—original draft, Writing—reviewing & editing. All authors have read and agreed to the published version of the manuscript.

Funding: This project has received funding from the European Union's Horizon 2020 research and innovation programme under the Marie Skłodowska-Curie Grant Agreement No. 101034403.

Institutional Review Board Statement: Not applicable.

Informed Consent Statement: Not applicable.

Data Availability Statement: All data generated or analyzed during this study are included in this manuscript, and further inquiries are available from the corresponding authors upon reasonable request.

Acknowledgments: During the preparation of the manuscript, the authors used ChatGPT (OpenAI source, GPT-5.2 model, accessed via https://chat.openai.com) to improve the writing style and readability of the manuscript. Additionally, certain illustrations incorporated into the graphical abstract and Figure 1 were generated with the assistance of ChatGPT (OpenAI source). After using this tool, the authors carefully reviewed and edited the content as needed and take full responsibility for the content of the published article.

Conflicts of Interest: The authors declare that they have no conflict of interest.

References

1. Dutta, S.; Gupta, B.; Srivastava, S.K.; Gupta, A.K. Recent advances on the removal of dyes from wastewater using various adsorbents: A critical review. *Mater. Adv.* **2021**, *2*, 4497–4531. [CrossRef]
2. Wang, Y.; Chen, T.; Zhang, X.; Mwamulima, T. Removal Study of Crystal Violet and Methylene Blue From Aqueous Solution by Activated Carbon Embedded Zero-Valent Iron: Effect of Reduction Methods. *Front. Environ. Sci.* **2021**, *9*, 2021. [CrossRef]
3. Talha, M.A.; Agwa, H.E.; Beltagi, A.M.; El-Mohsnawy, E.; Ali, A.S. Mechanistic insights into methylene blue biodegradation by Tetradesmus obliquus: A multimodal approach using absorption, fluorescence, and square wave voltammetry. *Sci. Rep.* **2025**, *15*, 32663. [CrossRef] [PubMed]
4. Al-Tohamy, R.; Ali, S.S.; Li, F.; Okasha, K.M.; Mahmoud, Y.A.G.; Elsamahy, T.; Jiao, H.; Fu, Y.; Sun, J. A critical review on the treatment of dye-containing wastewater: Ecotoxicological and health concerns of textile dyes and possible remediation approaches for environmental safety. *Ecotoxicol. Environ. Saf.* **2022**, *231*, 113160. [CrossRef] [PubMed]
5. Oladoye, P.O.; Ajiboye, T.O.; Omotola, E.O.; Oyewola, O.J. Methylene blue dye: Toxicity and potential elimination technology from wastewater. *Results Eng.* **2022**, *16*, 100678. [CrossRef]
6. Kolya, H.; Kang, C.-W. Toxicity of Metal Oxides, Dyes, and Dissolved Organic Matter in Water: Implications for the Environment and Human Health. *Toxics* **2024**, *12*, 111. [CrossRef] [PubMed]
7. Zhang, Z.; Lu, Y.; Gao, S.; Wu, S. Sustainable and Efficient Wastewater Treatment Using Cellulose-Based Hydrogels: A Review of Heavy Metal, Dye, and Micropollutant Removal Applications. *Separations* **2025**, *12*, 72. [CrossRef]
8. Aijaz, S.A.; Shafi, Z.; Shahid, M. Magnetized phyto-adsorbents for industrial dye removal: Functionalization and mechanistic insights for sustainable wastewater remediation. *RSC Adv.* **2026**, *16*, 758–777. [PubMed]
9. Aragaw, T.A.; Bogale, F.M. Biomass-Based Adsorbents for Removal of Dyes From Wastewater: A Review. *Front. Environ. Sci.* **2021**, *9*, 2021. [CrossRef]
10. Satyam, S.; Patra, S. Innovations and challenges in adsorption-based wastewater remediation: A comprehensive review. *Heliyon* **2024**, *10*, e29573. [CrossRef] [PubMed]
11. Tian, L.; Zhou, S.; Zhao, J.; Xu, Q.; Li, N.; Chen, D.; Li, H.; He, J.; Lu, J. Sulfonate-modified calixarene-based porous organic polymers for electrostatic enhancement and efficient rapid removal of cationic dyes in water. *J. Hazard. Mater.* **2023**, *441*, 129873. [PubMed]
12. Kumar, A.; Chang, D.W. Active Polymers Decorated with Major Acid Groups for Water Treatment: Potentials and Challenges. *Polymers* **2025**, *17*, 29.
13. Alkhaldi, H.; Alharthi, S.; Alharthi, S.; AlGhamdi, H.A.; AlZahrani, Y.M.; Mahmoud, S.A.; Amin, L.G.; Al-Shaalan, N.H.; Boraie, W.E.; Attia, M.S.; et al. Sustainable polymeric adsorbents for adsorption-based water remediation and pathogen deactivation: A review. *RSC Adv.* **2024**, *14*, 33143–33190. [CrossRef] [PubMed]
14. Phonlakan, K.; Meetam, P.; Chonlaphak, R.; Kongseng, P.; Chantarak, S.; Budsombat, S. Poly(acrylic acid-co-2-acrylamido-2-methyl-1-propanesulfonic acid)-grafted chitosan hydrogels for effective adsorption and photocatalytic degradation of dyes. *RSC Adv.* **2023**, *13*, 31002–31016. [PubMed]
15. Miao, C.; Huang, W.; Li, K.; Yang, Y. Highly efficient removal of adsorbed cationic dyes by dual-network chitosan-based hydrogel. *Environ. Res.* **2024**, *263*, 120195. [PubMed]
16. Li, X.; Li, K. Multifunctional pH-responsive carbon-based hydrogel adsorbent for ultrahigh capture of anionic and cationic dyes in wastewater. *J. Hazard. Mater.* **2023**, *449*, 131045. [PubMed]
17. Muhammadi, H.; Ghorbanloo, M.; Masami, M.; Yahiro, H. Adsorption of cationic dye from aqueous solutions by green pH responsive hydrogels based on poly(2-acrylamido-2-methyl-1-propanesulfonic acid). *Nanochemistry Res.* **2022**, *7*, 107–121.

18. Dhahir, S.A.; Braihi, A.J.; Habeeb, S.A. Comparative Analysis of Hydrogel Adsorption/Desorption with and without Surfactants. *Gels* **2024**, *10*, 251. [CrossRef] [PubMed]
19. Jastram, A.; Lindner, T.; Luebbert, C.; Sadowski, G.; Kragl, U. Swelling and Diffusion in Polymerized Ionic Liquids-Based Hydrogels. *Polymers* **2021**, *13*, 1834. [CrossRef] [PubMed]
20. Poornachandhra, C.; Jayabalakrishnan, R.M.; Prasanthrajan, M.; Balasubramanian, G.; Lakshmanan, A.; Selvakumar, S.; John, J.E. Cellulose-based hydrogel for adsorptive removal of cationic dyes from aqueous solution: Isotherms and kinetics. *RSC Adv.* **2023**, *13*, 4757–4774. [CrossRef] [PubMed]
21. Ibrahim, I.M.; Radwan, M.A.; El-Shahir, M.A.; Darwish, S.A.; Mostafa, N.Y. Effect of Electrostatic Interactions on the Dye Removal Behavior of Different Hydrogel-Based Materials. *Egypt. J. Chem.* **2023**, *66*, 257–261.
22. Shrivastava, G.; Singh, S.; Suvedi, D.; Sharma, A.; Rathi, N.; Sharma, G.; Sharma, A.; Nagraik, R. Bridging science and sustainability: Applications of nanomaterials in wastewater remediation. *Next Nanotechnol.* **2026**, *9*, 100470. [CrossRef]
23. Singh, H.; Dhanu, A.S.; Joshi, A.S.; Mijakovic, I.; Singh, P. Next-generation nanomaterials for environmental remediation: Smart design, hybrid materials and sustainable use. *Front. Chem.* **2026**, *14*, 2026. [CrossRef] [PubMed]
24. Arafat, E.A.; Hassan, M.A. A comprehensive review of bio-engineered nanofertilizers, nanopesticides, and nanobiochar for sustainable agriculture: Green synthesis, recent advances, challenges, and future outlooks. *Pestic. Biochem. Physiol.* **2026**, *220*, 107100. [CrossRef] [PubMed]
25. Zawidlak-Węgrzyńska, B.; Rydz, J. Polymer Nanoparticles in Medical Applications—Future Directions. *Nanomaterials* **2026**, *16*, 630. [CrossRef] [PubMed]
26. Homaeigohar, S. The Nanosized Dye Adsorbents for Water Treatment. *Nanomaterials* **2020**, *10*, 295. [CrossRef] [PubMed]
27. Choi, W.S.; Lee, H.-J. Nanostructured Materials for Water Purification: Adsorption of Heavy Metal Ions and Organic Dyes. *Polymers* **2022**, *14*, 2183. [CrossRef] [PubMed]
28. Tamer, T.; Abou-Krisha, M.; Omer, A.; Alhamzani, A.; Youssef, M.; Yousef, T.; Khalifa, R.; Salem, M.; Mohy-Eldin, M. Nano-Sulphonated Poly (glycidyl methacrylate)-Hexamethyl Pararosaniline chloride novel composite adsorbent development for treatment of dichromate and permanganate contaminated waste water. *Adsorption* **2024**, *30*, 877–890.
29. Khalifa, R.E.; Abou-Krisha, M.M.; Omer, A.M.; Alhamzani, A.G.; Youssef, M.E.; Yousef, T.A.; Tamer, T.M.; Salem, M.E.; Mohy-Eldin, M.S. Crystal violet removal from waste water by sulfonated poly (glycidyl methacrylate) nano-adsorbent: Optimization by response surface methodology, isotherms, kinetics, and thermodynamics studies. *Polym. Bull.* **2025**, *82*, 165–196.
30. Tamer, T.M.; Khalifa, R.E.; Abou-Krisha, M.M.; Omer, A.M.; Alhamzani, A.G.; Youssef, M.E.; Yousef, T.A.; Salem, M.E.; Mohy-Eldin, M.S. Dichromate Contaminated Water Treatment using Novel Crystal Violet Azo Dye-Sulphonated Poly (Glycidyl methacrylate) Nano-Composite Adsorbent. *Water Air Soil Pollut.* **2025**, *236*, 35.
31. Klučáková, M.; Havlíková, M.; Mravec, F.; Pekař, M. Diffusion of dyes in polyelectrolyte-surfactant hydrogels. *RSC Adv.* **2022**, *12*, 13242–13250. [CrossRef] [PubMed]
32. Banerjee, P.; Dinda, P.; Kar, M.; Uchman, M.; Mandal, T.K. Ionic Liquid Cross-Linked High-Absorbent Polymer Hydrogels: Kinetics of Swelling and Dye Adsorption. *Langmuir* **2023**, *39*, 9757–9772. [PubMed]
33. Zhang, X.; Zhang, K.; Shi, Y.; Xiang, H.; Yang, W.; Zhao, F. Surface engineering of multifunctional nanostructured adsorbents for enhanced wastewater treatment: A review. *Sci. Total Environ.* **2024**, *920*, 170951. [CrossRef] [PubMed]
34. Hosseinzadeh, H.; Khoshnood, N. Removal of cationic dyes by poly(AA-co-AMPS)/montmorillonite nanocomposite hydrogel. *Desalin. Water Treat.* **2016**, *57*, 6372–6383.
35. Elkony, A.; Ibrahim, A.G.; Abu El-Farah, M.H.; Abd-Elhai, F. Synthesis and characterization of (AAm-co-AHPS)/MMT hydrogel composites for the efficient capture of methylene blue from aqueous solution. *Al-Azhar Bull. Sci.* **2020**, *2020*, 31–46.
36. Kasbaji, M.; Mennani, M.; Grimi, N.; Oubenali, M.; Mbarki, M.; El Zakhem, H.; Moubarik, A. Adsorption of cationic and anionic dyes onto coffee grounds cellulose/sodium alginate double-network hydrogel beads: Isotherm analysis and recyclability performance. *Int. J. Biol. Macromol.* **2023**, *239*, 124288. [PubMed]
37. Altaleb, H.A. Effective removal of hazardous cationic dye from polluted water using sulfonated copolymer hydrogel: Synthesis, nonlinear isotherm, and kinetics investigation. *J. Saudi Chem. Soc.* **2024**, *28*, 101852. [CrossRef]
38. Altaleb, H.A.; Nasser, A.M.; Thamer, B.M. Sulfonated/carboxylated chitosan hydrogels for selective removal of cationic dyes. *Mater. Chem. Phys.* **2026**, *351*, 131989.
39. Yuan, T.; Zhang, X.; Zhang, D.; Wang, M. Removal of Cationic Malachite Green Dyes in Waster Water by PGS-AMPS-AM Hydrogel. In *Innovative Computing Vol 2–Emerging Topics in Future Internet*; Hung, J.C., Chang, J.-W., Pei, Y., Eds.; Springer Nature: Singapore, 2023; pp. 407–415.

Disclaimer/Publisher's Note: The statements, opinions and data contained in all publications are solely those of the individual author(s) and contributor(s) and not of MDPI and/or the editor(s). MDPI and/or the editor(s) disclaim responsibility for any injury to people or property resulting from any ideas, methods, instructions or products referred to in the content.